1971

Radial surface waves on piezoelectric substrates

Clifford Keith Day
Iowa State University

72-5192

DAY, Clifford Keith, 1940-
  RADIAL SURFACE WAVES ON PIEZOELECTRIC
  SUBSTRATES.

  Iowa State University, Ph.D., 1971
  Engineering, electrical

University Microfilms, A XEROX Company , Ann Arbor, Michigan

Radial surface waves on piezoelectric substrates

by

Clifford Keith Day

A Dissertation Submitted to the

Graduate Faculty in Partial Fulfillment of

The Requirements for the Degree of

DOCTOR OF PHILOSOPHY

Major Subject: Electrical Engineering

Approved:

In Charge of Major Work

For the Major Department

For the Graduate College

Iowa State University
Ames, Iowa

1971

PLEASE NOTE:

Some Pages have indistinct
print. Filmed as received.

TABLE OF CONTENTS

LIST OF ILLUSTRATIONS

LIST OF TABLES

LIST OF SYMBOLS

α — decay constant

ω — angular frequency

k — wave number

ζ, ψ, η — displacement potentials

g — determinant of metric matrix

ρ — mass density

ϵ_o — permitivity of free space

ϕ — electric scalar potential

E^i — electric field intensity

D^i — electric flux density

x^i — coordinate axes

$\varkappa_S^{ij}$ — dielectric constant at constant strain

S^{ij} — strain tensor

T^{ij} — stress tensor

C_{ij} — elastic stiffness matrix

g_{ij} — metric tensor

e^{ijk} — piezoelectric constant

$C_E^{ijk\ell}$ — elastic stiffness constant at constant electric field

I. INTRODUCTION

A. Background

Microwave ultrasonics in general and surface waves in particular
have been the subjects of intense study during recent years. There
appear to be many reasons for this wide-spread interest. Perhaps the
most important, however, is the small device sizes which result because
acoustic waves are slower than electromagnetic waves by approximately
five orders of magnitude. As van den Heuvel (30) suggests, the goal
today is to "pack all of electronics onto a tiny speck of silicon no
larger than a grain of sand."

Surface waves offer the additional advantage of accessibility when
compared to the long-studied bulk waves. In a surface wave device, all
of the traveling energy is available to be sensed, mixed, or amplified
along its entire path of travel. Also, surface wave techniques are
compatible with microwave and integrated circuit technologies.

Smith and Damon (23) have provided an excellent bibliography that
contains many papers describing the development of surface wave
technology from its analytical inception by Rayleigh (22) nearly 100
years ago to the recent past. Therefore, no attempt will be made to
detail this development here.

Considerable effort has been devoted to the development of trans-
ducers to generate acoustical waves in materials. Nearly 100 recent
papers are cited in this area alone by Smith and Damon (23). Bradfield
(4,5) classifies ultrasonic transducers into 22 separate groups under
the main headings of sources, reversible devices, and detectors.

Childs (7) compares microwave frequency transducers and offers a new device, the strip line electrically resonant transducer, for operation in the microwave region of the acoustical spectrum. He anticipates use of the strip line transducer at frequencies well above the photo mask limit (approximately 800 MHz) that restricts the use of surface wave transducers. Most surface wave devices operate below this limit due to the difficulty of making closely spaced conducting electrodes for inter-digital transducers. However, recent literature (17) describes 2.5 GHz transducers constructed by electron beam techniques. Using these techniques, Budreau and Carr (6) were able to measure surface wave attenuation at 1.533 GHz.

The most common surface wave transducer is the set of interdigital electrodes deposited on piezoelectric substrates (24). Using parallel electrodes, this transducer produces at least 6 db insertion loss due to equal amounts of acoustic energy propagating in the two directions perpendicular to the electrodes. Collins and others (8) have reported on a special interdigital transducer design to radiate in essentially one direction. Using properly phased electrodes which cancel the "reverse" traveling wave, low insertion losses were achieved. This technique has the inherent disadvantage, however, of narrow bandwidth. Worley and Matthews (31) use quarter wave spaced electrodes and a "meandering" ground line to achieve some improvement in the bandwidth of their unidirectional transducer.

B. Motivation and Scope

The desire to reduce insertion loss by intercepting most of the

radiated energy from interdigital transducers was the driving force behind this research. One transducer configuration which offers this possibility is the point source surface wave transmitter with receiving electrodes arranged to intercept all of the acoustical energy. Figure 1 shows schematically how such a device might operate. The transmitting and receiving transducers could consist of concentric metal electrodes on a piezoelectric substrate spaced to give the desired delay time.

It is the purpose of this thesis to report on the research related to the radial surface waves generated by concentric metal electrodes on certain piezoelectric substrates. The investigation includes a mathematical analysis that will completely characterize the particle displacement and electric field components of the traveling waves. In addition, an experimental study is described and results are presented confirming the validity of the mathematical model.

PIEZOELECTRIC SUBSTRATE

TRANSMIT ELECTRODES

RECEIVE ELECTRODES
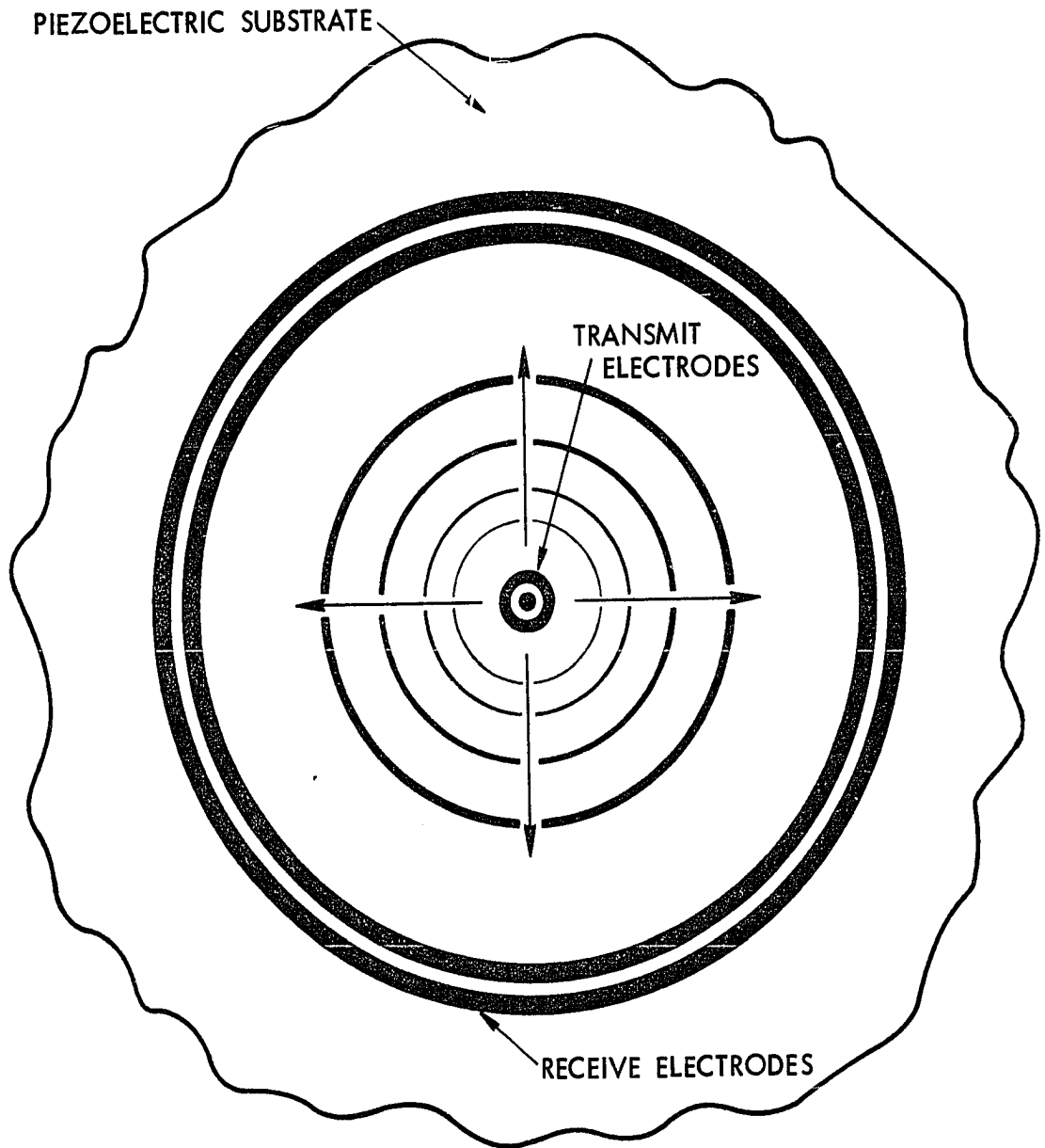
Fig. 1. Radial surface waves generated on a piezoelectric substrate.

II. THEORETICAL ANALYSIS

The physical laws that provide the basis for the mathematical development include Newton's second law of motion and Maxwell's equations. It is necessary to consider Maxwell's equations in the analysis because of the coupling between electric fields and particle displacements produced by piezoelectric constants for the materials of interest.

A. Governing Equations

In Cartesian coordinates, Newton's second law of motion for elastic waves in materials can be written as (13):

$$\rho \ddot{u}^{i\,'} = \frac{\partial T^{ij\,'}}{\partial x^{j\,'}} \tag{1}$$

where the tensor index notation described by Aris (2) will be used. The dots specify differentiation with respect to time, ρ is the material density that is assumed to be homogenous, $u^{i\,'}$ is the particle displacement parallel to the $x^{i\,'}$ coordinate axis, and $T^{ij\,'}$ is the stress tensor in the Cartesian (primed) coordinate system.

Maxwell's divergence of the electric flux density for a charge free region will be used

$$\frac{\partial D^{i\,'}}{\partial x^{i\,'}} = 0 \tag{2}$$

As a further restriction on Maxwell's equations, the electrostatic approximation will be assumed to apply. This is quite adequate since the transducer region is very short when compared to an electrical wavelength. As a consequence of this assumption, the curl of the

electric field is zero and the gradient of a scalar electric potential

can represent the electric field or

$$E_i{}' = - \frac{\partial \phi}{\partial x^{i'}} \tag{3}$$

where ϕ is the scalar electric potential.

The indices i and j of the above equations, as well as the indices

of all equations which follow, will take on the values of 1, 2, and 3

corresponding to the three coordinate axes. Using the Einstein

summation convention (19), an index appearing once in the superscript

position and once in the subscript position of the same term is considered

a dummy index and specifies summation over the index range. An index

appearing only once in a term is a free index and can assume any value

in the range (1, 2, or 3). Therefore, Equation 1 represents three

equations for the particle displacements $u^{1'}$, $u^{2'}$, and $u^{3'}$.

The constitutive relationships specify the characteristics of the

medium through which the waves must propagate. For piezoelectric media,

piezoelectric constants in these equations couple Newton's second law

and Maxwell's equations. The constitutive relationships of concern

here are

$$T^{ij'} = C_E^{ijk\ell'} S_{k\ell}' - e^{kij'} E_k' \tag{4a}$$

$$D^{i'} = e^{ijk'} S_{jk}' + \epsilon_o \varkappa_S^{ij'} E_j' \tag{4b}$$

where $C_E^{ijk\ell'}$ is the fourth rank tensor form of the material elastic

constants at constant electric field, $S^{k\ell'}$ is the second rank strain

tensor, $e^{kij'}$ and $e^{ijk'}$ are third rank piezoelectric constants, $\kappa_s^{ij'}$ is the relative dielectric constant at constant strain, and ϵ_o is the permittivity of free space (8.854×10^{-12} farad per meter).

The strain tensor can be expressed in terms of particle displacement or

$$S_{ij} = \frac{1}{2} \left(\frac{\partial u_i'}{\partial x^{j'}} + \frac{\partial u_j'}{\partial x^{i'}} \right) \tag{5}$$

It is now possible to collect all of the preceeding equations together into four coupled partial differential equations in terms of three displacement quantities, $u^{i'}$, and the scalar electric potential, ϕ. These, along with the appropriate boundary conditions, could completely describe wave propagation in piezoelectric media with respect to Cartesian coordinates.

1. Transforming to curvilinear coordinates

For the electrode configuration suggested by Figure 1, it is necessary that the wave fronts be cylindrically symmetrical. Therefore, the mathematical model should be constructed in cylindrical coordinates.

Martin (18) points to the value of using true tensors in the analysis of problems involving coordinate system other than Cartesian. The notation suggested by Martin and techniques described by Aris (2) were followed during the transformation of the fundamental equations from Cartesian to curvilinear coordinates.

a. General   The desire, as stated by Aris, is "to represent physical entities in such a way that when changing the coordinate system our description changes in such a way that we are sure the

entity itself has not changed." This requires a distinction between contravariant and covariant tensors. The distinction is not necessary in the Cartesian system since the behavior of each tensor under simple rotational transformations is identical. Contravariant tensors are identified by one or more superscripts while subscripts denote covariant tensors.

In general, a contravariant tensor of rank one (vector) will transform according to the equation

$$a^{i'} = \frac{\partial x^{i'}}{\partial x^j} a^j \tag{6}$$

where $a^{i'}$ is a contravariant vector in the Cartesian system and a^j represents the vector in a curvilinear coordinate system. Higher rank tensors transform into curvilinear coordinates in a similar manner but with additional partial derivatives appearing as products in the above equation.

The covariant first rank tensor transforms according to

$$a_i' = \frac{\partial x^j}{\partial x^{i'}} a_j \tag{7}$$

with additional partials required for higher rank covariant tensor transformations.

Covariant and contravariant tensors are related by the metric tensor, g_{ij}, as

$$a_i = g_{ij} a^j . \tag{8}$$

The metric tensor (see Aris (2), page 142) relates distance to the infinitesimal coordinate increments.

It is also convenient to introduce the Christoffel symbol of the second kind defined by

$$\{_{j\ k}^{\ i}\} = \frac{1}{2} g^{ip} \left(\frac{\partial g_{pj}}{\partial x^k} + \frac{\partial g_{pk}}{\partial x^j} - \frac{\partial g_{jk}}{\partial x^p} \right) \tag{9}$$

It is now possible to define the covariant derivative of a contravariant tensor, denoted by a comma followed by the proper index. As an example, the covariant derivative of the doubly contravariant stress tensor would be

$$T^{ij}_{\ ,j} = \frac{1}{g^{\frac{1}{2}}} \frac{\partial}{\partial x^j}(g^{\frac{1}{2}}T^{ij}) + \{_{j\ k}^{\ i}\} T^{jk} \tag{10}$$

where g is the determinant of the matrix whose elements are the values of the metric tensor, g_{ij}. Each of the other quantities have been previously defined.

Equations 3 through 10 provide the basic for a general representation of Newton's second law in curvilinear coordinates:

$$\rho \frac{\partial^2 u^i}{\partial t^2} = \frac{1}{g^{\frac{1}{2}}} \frac{\partial}{\partial x^j} \left[g^{\frac{1}{2}} \frac{c^{ijk\ell}}{2} \left(g_{km} \left[\frac{\partial u^m}{\partial x^\ell} + \{_{\ell\ n}^{\ m}\} u^n \right] \right. \right.$$

$$\left. + g_{\ell m} \left[\frac{\partial u^m}{\partial x^k} + \{_{k\ n}^{\ m}\} u^n \right] \right) + g^{\frac{1}{2}} e^{kij} \frac{\partial \phi}{\partial x^k} \right]$$

$$+ \{_{r\ s}^{\ i}\} \left[\frac{c^{rsk\ell}}{2} \left(g_{km} \left[\frac{\partial u^m}{\partial x^\ell} + \{_{\ell\ n}^{\ m}\} u^n \right] \right. \right.$$

$$\left. \left. + g_{\ell m} \left[\frac{\partial u^m}{\partial x^k} + \{_{k\ n}^{\ m}\} u^n \right] \right) + e^{krs} \frac{\partial \phi}{\partial x^k} \right] \tag{11}$$

where i, j, k, ℓ, m, n, r, s = 1, 2, 3. This equation represents three

coupled equations for the three displacements of u^1, u^2, and u^3 and includes the electric potential, ϕ. It is a completely general expression of Newton's second law for piezoelectric media and can represent bulk or surface waves, depending on the conditions placed on the problem.

The divergence of the electric flux density in curvilinear coordinates becomes

$$0 = \frac{1}{g^{\frac{1}{2}}} \frac{\partial}{\partial x^p} \left[g^{\frac{1}{2}} e^{pk\ell} \left(g_{km} \left[\frac{\partial u^m}{\partial x^\ell} + \{ {}^m_{\ell\,n} \} u^n \right] \right. \right.$$
$$\left. \left. + g_{\ell m} \left[\frac{\partial u^m}{\partial x^k} + \{ {}^m_{k\,n} \} u^n \right] \right) - \epsilon_o g^{\frac{1}{2}} \varkappa^{pq} \frac{\partial \phi}{\partial x^q} \right] \qquad (12)$$

where k, ℓ, m, n, p, q = 1, 2, 3.

    <u>b.</u> <u>Cylindrical</u>   Using the notation scheme suggested by Martin (18), the following symbols will represent the coordinate systems of interest:

$$(x^{1'}, x^{2'}, x^{3'}) - \text{Cartesian axes (x, y, z)}$$

$$(x^1, x^2, x^3) \quad - \text{cylindrical coordinates (r, } \theta, \text{ z)}$$

The partials of Equations 6 and 7 may be evaluated from the following relationships between Cartesian and cylindrical coordinates.

$$x^{1'} = x^1 \cos x^2 \qquad (13a)$$

$$x^{2'} = x^1 \sin x^2 \qquad (13b)$$

$$x^{3'} = x^3 \qquad (13c)$$

and

$$x^1 = \{(x^{1'})^2 + (x^{2'})^2\}^{\frac{1}{2}} \tag{14a}$$

$$x^2 = \tan^{-1}(x_2'/x_1') \tag{14b}$$

$$x^3 = x^{3'} \tag{14c}$$

For cylindrical coordinates the metric tensor has the following values

$$g_{11} = g_{33} = 1 \tag{15a}$$

$$g_{22} = (x^1)^2 \tag{15b}$$

$$g_{ij}(i \neq j) = 0 \tag{15c}$$

Therefore, the value of g for Equation 10 is

$$g = (x^1)^2. \tag{16}$$

Using Equations 15 in Equation 9 produces three non-zero Christoffel symbols

$$\{^{\ 1}_{2\ 2}\} = -x^1 \tag{17a}$$

$$\{^{\ 2}_{1\ 2}\} = \{^{\ 2}_{2\ 1}\} = \frac{1}{x^1} \tag{17b}$$

while all others are zero.

2. Problem formulation in cylindrical coordinates

The first conditions placed on the problem relate to the coordinate system shown in Figure 2. The wave is assumed to propagate in the x^1 or r direction, to decay in the x^3 or z direction, and to remain uniform in the x^2 or θ direction. Uniformity in the θ direction implies all derivatives with respect to the x^2 dimension are zero. The propagation and decay directions will dictate a special form for the solutions to

SEMI-INFINITE PIEZOELECTRIC SUBSTRATE IN $x^3 < 0$
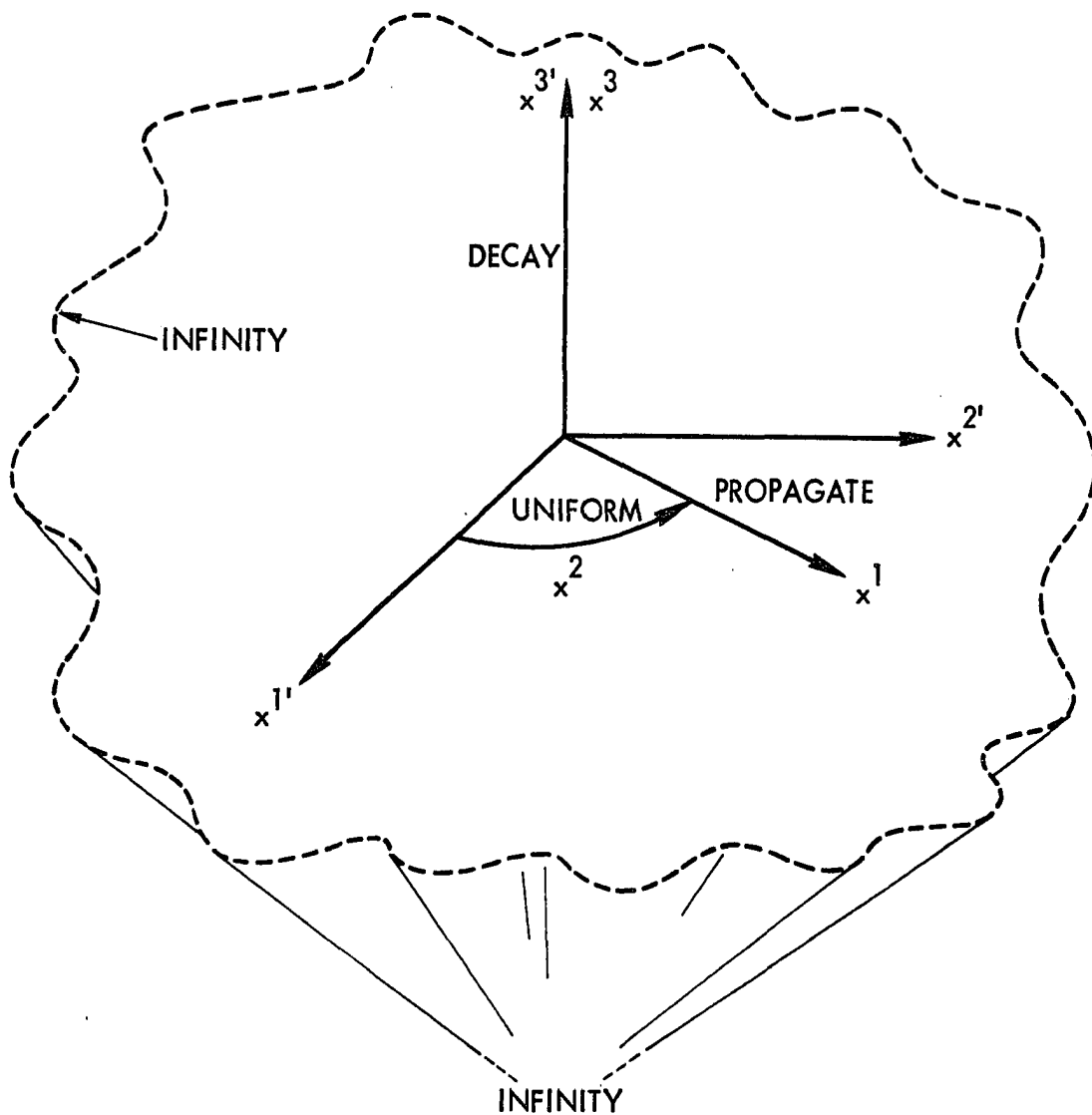
Fig. 2. Coordinate systems and restrictions under which waves are assumed to propagate.

the governing equations.

Next, it is necessary to select the crystal symmetry to be imposed on the problem. Since it is important that the wave fronts remain circular when viewed down the x^3 axis, the wave velocity must be the same for all values of θ. This implies transverse isotropy (20), i.e., an invariance of the parameters of permittivity, piezoelectricity, and elasticity when subjected to arbitrary rotations about the x^3 axis. The four crystal classes meeting the criteria for this problem are 4, 4mm, 6, and 6mm. Table 1 lists materials for each of these crystal classes. These are only a few of the materials that appear with their properties in Landolt-Börnstein (15,16). The 6mm crystal class was chosen as the symmetry for this problem because of the availability of a lead-zirconate-titanate ferroelectric ceramic, PZT-5A[1], for the experimental portion of the program. Polarized ferroelectric ceramics possess the properties of transverse isotropy (12) or the 6mm symmetry class. The analysis would hold equally well for the other symmetry classes noted above.

The effects of 6mm symmetry, as discussed by Mason (19), on the macroscopic properties of permittivity, piezoelectricity, and elasticity are summarized in Figure 3. Matrix notation (21) is used as a matter of convenience. The correspondence between the indices of tensor symbols and matrix symbols are as follows:

tensor notation	11	22	33	23,32	13,31	12,21
matrix notation	1	2	3	4	5	6

---

[1]Clevite Corporation trademark.

14

Table 1. Typical materials with the property of transverse
isotropy and the physical constants for PZT-5A.

Class	Material	Class	Material
4	Chrysazin $C_{14}H_8O_4$ Di-calcium strontium propionate $Ca_2Sr(C_2H_5CO_2)_6$ Potassium strontium niobate $KSr_2Nb_5O_{15}$	6	Lithium iodate $LiIO_3$ Lithium potassium sulfate $LiKSO_4$ Sodium aluminum silicate $NaAlSiO_4$
4mm	Barium titanate $BaTiO_3$ (single crystal) Potassium lithium niobate $K_3Li_2Nb_5O_{15}$ Potassium tantalate niobate $KTaNbO_3$ Strontium barium niobate $SrBaNb_2O_6$	6mm	Cadmium selenide CdSe Cadmium sulfide CdS Lead zirconate titanate PZT-5A Zinc Oxide ZnO

Physical Constants for PZT-5A

$c_{11}^E = 1.21 \times 10^{11} n/m^2$ $\qquad e_{15} = 12.3\ c/m^2$ $\qquad \varkappa_{11}^S = 916$

$c_{13}^E = 0.752 \times 10^{11} n/m^2$ $\qquad e_{31} = -5.4\ c/m^2$ $\qquad \varkappa_{33}^S = 830$

$c_{33}^E = 1.11 \times 10^{11} n/m^2$ $\qquad e_{33} = 15.8\ c/m^2$ $\qquad \rho = 7750\ kg/m^3$

$c_{44}^E = 0.211 \times 10^{11} n/m^2$

$$
\begin{array}{ccccccc|ccc}
C_{11} & C_{12} & C_{13} & \bullet & \bullet & \bullet & & \bullet & \bullet & e_{13} \\
C_{12} & C_{11} & C_{13} & \bullet & \bullet & \bullet & & \bullet & \bullet & e_{13} \\
C_{13} & C_{13} & C_{33} & \bullet & \bullet & \bullet & & \bullet & \bullet & e_{33} \\
\bullet & \bullet & \bullet & C_{44} & \bullet & \bullet & & \bullet & e_{15} & \bullet \\
\bullet & \bullet & \bullet & \bullet & C_{44} & \bullet & & e_{15} & \bullet & \bullet \\
\bullet & \bullet & \bullet & \bullet & \bullet & \frac{1}{2}(C_{11}-C_{12}) & & \bullet & \bullet & \bullet \\
\hline
\bullet & \bullet & \bullet & \bullet & e_{15} & \bullet & & \varkappa_{11} & \bullet & \bullet \\
\bullet & \bullet & \bullet & e_{15} & \bullet & \bullet & & \bullet & \varkappa_{11} & \bullet \\
e_{13} & e_{13} & e_{33} & \bullet & \bullet & \bullet & & \bullet & \bullet & \varkappa_{33}
\end{array}
$$

(a) Cartesian coordinates.

$$
\begin{array}{ccccccc|ccc}
C_{11} & (x^1)^2 C_{12} & C_{13} & \bullet & \bullet & \bullet & & \bullet & \bullet & e_{13} \\
(x^1)^2 C_{12} & (x^1)^4 C_{11} & (x^1)^2 C_{13} & \bullet & \bullet & \bullet & & \bullet & \bullet & (x^1)^2 e_{13} \\
C_{13} & (x^1)^2 C_{13} & C_{33} & \bullet & \bullet & \bullet & & \bullet & \bullet & e_{33} \\
\bullet & \bullet & \bullet & (x^1)^2 C_{44} & \bullet & \bullet & & \bullet & (x^1)^2 e_{15} & \bullet \\
\bullet & \bullet & \bullet & \bullet & C_{44} & \bullet & & e_{15} & \bullet & \bullet \\
\bullet & \bullet & \bullet & \bullet & \bullet & \frac{(x^1)^2}{2}(C_{11}-C_{12}) & & \bullet & \bullet & \bullet \\
\hline
\bullet & \bullet & \bullet & \bullet & e_{15} & \bullet & & \varkappa_{11} & \bullet & \bullet \\
\bullet & \bullet & \bullet & (x^1)^2 e_{15} & \bullet & \bullet & & \bullet & (x^1)^2 \varkappa_{11} & \bullet \\
e_{13} & (x^1)^2 e_{13} & e_{33} & \bullet & \bullet & \bullet & & \bullet & \bullet & \varkappa_{33}
\end{array}
$$

(b) Cylindrical coordinates.

Fig. 3. The unique crystal properties for 6mm symmetry referred to the conventional crystallographic axes.

For example, C_{1223} becomes C_{64} and e_{113} becomes e_{15}.

The unique non-zero values of the physical properties in both the Cartesian and cylindrical systems are shown in Figure 3. Dots represent the zero values of the properties as discussed by Mason (19). Martin (18) describes the relationship between the cylindrical and Cartesian forms of second, third, and fourth rank tensors and shows that the number of unique parameters increases for the cylindrical coordinate system.

Newton's and Maxwell's equations (11 and 12) can now be simplified with the information provided in Figures 2 and 3 and Equations 13 through 17. Newton's equations become:

$$\rho \frac{\partial^2 u^1}{\partial t^2} = C'_{1111} \left[\frac{\partial^2 u^1}{\partial x^1 \partial x^1} + \frac{1}{x^1} \frac{\partial u^1}{\partial x^1} - \frac{u^1}{(x^1)^2} \right]$$

$$+ C'_{1313} \left[\frac{\partial^2 u^1}{\partial x^3 \partial x^3} + \frac{\partial^2 u^3}{\partial x^1 \partial x^3} \right] + C'_{1133} \frac{\partial^2 u^3}{\partial x^1 \partial x^3}$$

$$+ (e'_{113} + e'_{311}) \frac{\partial^2 \phi}{\partial x^1 \partial x^3} \tag{18a}$$

$$\rho \frac{\partial^2 u^2}{\partial t^2} = C'_{1212} \left[\frac{\partial^2 u^2}{\partial x^1 \partial x^1} + \frac{3}{x^1} \frac{\partial u^2}{\partial x^1} \right] + C'_{2323} \frac{\partial^2 u^2}{\partial x^3 \partial x^3} \tag{18b}$$

$$\rho \frac{\partial^2 u^3}{\partial t^2} = C'_{1133} \left[\frac{\partial^2 u^1}{\partial x^1 \partial x^3} + \frac{1}{x^1} \frac{\partial u^1}{\partial x^3} \right] + C'_{1313} \left[\frac{\partial^2 u}{\partial x^1 \partial x^3} + \frac{\partial^2 u^3}{\partial x^1 \partial x^1} \right]$$

$$+ \frac{1}{x^1} \frac{\partial u^1}{\partial x^3} + \frac{1}{x^1} \frac{\partial u^3}{\partial x^1} \right] + C'_{3333} \frac{\partial^2 u^3}{\partial x^3 \partial x^3}$$

$$+ e'_{113} \left[\frac{\partial^2 \phi}{\partial x^1 \partial x^1} + \frac{1}{x^1} \frac{\partial \phi}{\partial x^1} \right] + e'_{333} \frac{\partial^2 \phi}{\partial x^3 \partial x^3} \tag{18c}$$

The divergence of the electric flux density becomes:

$$0 = e'_{113} \left[\frac{\partial^2 u^1}{\partial x^1 \partial x^3} + \frac{1}{x^1} \frac{\partial u^1}{\partial x^3} + \frac{1}{x^1} \frac{\partial u^3}{\partial x^1} + \frac{\partial^2 u^3}{\partial x^1 \partial x^1} \right]$$

$$+ e'_{311} \left[\frac{\partial^2 u^1}{\partial x^1 \partial x^3} + \frac{1}{x^1} \frac{\partial u^1}{\partial x^3} \right] + e'_{333} \frac{\partial^2 u^3}{\partial x^3 \partial x^3}$$

$$- \varepsilon_0 \kappa'_{11} \left[\frac{\partial^2 \phi}{\partial x^1 \partial x^1} + \frac{1}{x^1} \frac{\partial \phi}{\partial x^1} \right] - \varepsilon_0 \kappa'_{33} \frac{\partial^2 \phi}{\partial x^3 \partial x^3} \qquad (18d)$$

where the primes on the material constants indicate that the matrix components given in Figure 3, referred to Cartesian crystallographic axes, are being used.

Inspection of Equations 18 reveals coupling between 18a, c, and d since u^1, u^3, and ϕ appears in each of these equations. Equation 18b involves only the u^2 component of particle displacement and is, therefore, decoupled from the other three equations. The conditions for decoupling are discussed by Koerber (14). To insure complete decoupling, it is necessary to consider the appropriate boundary conditions. As noted in Figure 2, it is assumed that a piezoelectric substrate fills the lower half space, $x^3 < 0$, and free space exists above the piezoelectric medium. Hence, the boundary conditions would be:

1. Continuous electric potential across the boundary $x^3 = 0$, $\phi(0^+) = \phi(0^-)$.

2. Continuous electric flux density, $D^3(0^+) = D^3(0^-)$.

3. The components of the stress vector vanish at $x^3 = 0$.

For the free space region, $x^3 > 0$, it is necessary to solve Laplace's equation in cylindrical coordinates (26).

$$\frac{\partial^2 \phi}{\partial x^1 \partial x^1} + \frac{1}{r}\frac{\partial \phi}{\partial x^1} + \frac{\partial^2 \phi}{\partial z \partial z} = 0 \tag{19}$$

When the boundary conditions are applied, only conditions 2 and 3 can provide coupling for the dependent variables u^1, u^2, u^3, and ϕ. Using the constitutive relationships of Equations 4 and the equations for electric field and strain, Equations 3 and 5, respectively, these conditions become:

$$-\epsilon_o \frac{\partial \phi}{\partial x^3}\bigg|_{x^3=0} = \{e'_{311}[\frac{\partial u^1}{\partial x^1} + \frac{u^1}{x^1}] + e'_{333}\frac{\partial u^3}{\partial x^3}$$

$$-\epsilon_o \varkappa'_{33}\frac{\partial \phi}{\partial x^3}\}\bigg|_{x^3=0} \tag{20a}$$

for the normal component of flux density and

$$T^{13} = 0 = \{C'_{1313}[\frac{\partial u^1}{\partial x^3} + \frac{\partial u^3}{\partial x^1}] + e'_{113}\frac{\partial \phi}{\partial x^1}\}\bigg|_{x^3=0} \tag{20b}$$

$$T^{23} = 0 = C'_{2323}\frac{\partial u^2}{\partial x^3}\bigg|_{x^3=0} \tag{20c}$$

$$T^{33} = 0 = \{ C'_{1313} [\frac{\partial u^1}{\partial x^3} + \frac{\partial u^3}{\partial x^1}] + e'_{113} \frac{\partial \phi}{\partial x^1} \} \Big|_{x^3 = 0} \qquad (20d)$$

for the zero components of stress. Once again, u^1, u^3, and ϕ are coupled while u^2 is decoupled. Hence, two mode groups exist and will be referred to as (u^1, u^3, ϕ), the radial mode, and (u_2).

As a matter of convenience, the coupled Equations 18a, c, and d are rewritten below using the matrix notation for the physical properties and the symbols r and z for the cylindrical coordinate parameters x^1 and x^3. Also, u_r and u_z replace u^1 and u^3, respectively.

$$\rho \ddot{u}_r = C_{11} [\frac{\partial^2 u_r}{\partial r^2} + \frac{1}{r} \frac{\partial u_r}{\partial r} - \frac{u_r}{r^2}] + C_{44} \frac{\partial^2 u_r}{\partial z^2}$$

$$+ (C_{44} + C_{13}) \frac{\partial^2 u_z}{\partial r \partial z} + (e_{15} + e_{31}) \frac{\partial^2 \phi}{\partial r \partial z} \qquad (21a)$$

$$\rho \ddot{u}_z = (C_{13} + C_{44}) [\frac{\partial^2 u_r}{\partial r \partial z} + \frac{1}{r} \frac{\partial u_r}{\partial z}] + C_{44} [\frac{\partial^2 u_z}{\partial r^2} + \frac{1}{r} \frac{\partial u_z}{\partial r}]$$

$$+ C_{33} \frac{\partial^2 u_z}{\partial z^2} + e_{15} [\frac{\partial^2 \phi}{\partial r^2} + \frac{1}{r} \frac{\partial \phi}{\partial r}] + e_{33} \frac{\partial^2 \phi}{\partial z^2} \qquad (21b)$$

$$0 = (e_{15} + e_{31}) [\frac{\partial^2 u_r}{\partial r \partial z} + \frac{1}{r} \frac{\partial u_r}{\partial z}] + e_{15} [\frac{\partial^2 u_z}{\partial r^2} + \frac{1}{r} \frac{\partial u_z}{\partial r}]$$

$$+ e_{33} \frac{\partial^2 u_z}{\partial z^2} - \epsilon_0 \kappa_{11} [\frac{\partial^2 \phi}{\partial r^2} + \frac{1}{r} \frac{\partial \phi}{\partial r}] - \epsilon_0 \kappa_{33} \frac{\partial^2 \phi}{\partial z^2} \qquad (21c)$$

These three equations describe the motion of radial waves in the region $z < 0$. Rewriting Equation 19 to include the new notation

$$\frac{\partial^2 \phi}{\partial r^2} + \frac{1}{r} \frac{\partial \phi}{\partial r} + \frac{\partial^2 \phi}{\partial z^2} = 0 \qquad (22)$$

Again this describes the electric potential in the region $z > 0$ that is associated with the traveling radial surface wave.

The problem now is to find the complete solutions for the particle displacements, u_r and u_z, and the electric potential ϕ. This comprises the next section.

B. Field and Displacement Solutions

1. Mathematical representation for solutions

Ewing, Jardetzky, and Press (10) discuss cylindrical waves in isotropic media. They suggest replacing particle displacements by the sum of the gradient of a scalar potential and the curl of a vector potential. Using this technique, they are able to reduce the two coupled equations of motion involving particle displacements to two separate wave equations for the displacement potentials. In this way, solutions for the particle displacements are immediately suggested.

A similar procedure was followed in searching for solutions to Equations 21. The following substitutions were made for the particle displacements in cylindrical coordinates:

$$u_r = \frac{\partial \zeta}{\partial r} - \frac{\partial \psi}{\partial z} \qquad (23a)$$

$$u_z = \frac{\partial \zeta}{\partial z} + \frac{1}{r} \frac{\partial}{\partial r} (r\psi) \qquad (23b)$$

where ζ is a scalar displacement potential and ψ is the θ component of a vector displacement potential. In addition, it was necessary to

substitute another function, η, for ψ in order to obtain the desired form

for the differential equations involving the potentials

$$\psi = -\frac{\partial \eta}{\partial r} \tag{23c}$$

The resulting differential equations suggest that Bessel's equation

of zero order is the governing equation for the r dependence of the

function ζ, η, and ϕ. Using Harrington's (11) notation and denoting

general solutions to Bessel's equation by $B_o(kr)$, it is an easy matter

to determine the form of the solutions for the particle displacements by

taking the derivatives indicated in Equations 23. It is found that the

u_r component of displacement has a $B_1(kr)$ dependence while u_z and ϕ are

each functions of $B_o(kr)$ where k is the wave number.

It is necessary for the solutions to describe surface wave propa-

gation. In order for the conditions of Figure 2 to hold, that is,

r-propagating, θ-uniform, and z-decay, the solutions must have the

following form in the region z < 0:

$$u_r = A_r B_1(kr) \exp (\alpha kz + j\omega t) \tag{24a}$$

$$u_z = A_z B_o(kr) \exp (\alpha kz + j\omega t) \tag{24b}$$

$$\phi = A_\phi B_o(kr) \exp (\alpha kz + j\omega t) \tag{24c}$$

where A_r, Z_z, and A_ϕ are arbitrary amplitude constants, α is a decay

constant, k is the wave number, ω is the angular frequency, and t is

time.

The $B_1(kr)$ and $B_o(kr)$ in Equations 24 must represent traveling waves

and, therefore, must be Hankel functions (11) of the first (inward

traveling waves) or second (outward traveling waves) kind. This conclusion assumes the wave number, k, to be real. If k were complex, the traveling waves would be attenuated in the direction of travel. For purely imaginary k, modified Bessel functions result which represent evanescent-type fields, as described by Harrington. For this problem, k will be assumed to be real and the decay constant, α, will be allowed to take on complex values.

Most of the mathematical methods that follow are quite similar to those used by Tseng and White (29) and Spaight (25) for the analysis of plane waves in Cartesian coordinates. Tseng and White considered the general problem of piezoelectric surface waves on hexagonal crystals while Spaight investigated these waves on LiNbO₃.

If the solutions of Equations 24 are put into Equations 21, it is possible to obtain the following simplified forms:

$$(\rho v^2 - c_{11} + c_{44}\alpha^2) A_r - \alpha(c_{44} + c_{13}) A_z$$

$$- \alpha(e_{15} + e_{31}) A_\phi = 0 \tag{25a}$$

$$\alpha(c_{44} + c_{13}) A_r + (\rho v^2 - c_{44} + c_{33}\alpha^2) A_z$$

$$+ (e_{33}\alpha^2 - e_{15}) A_\phi = 0 \tag{25b}$$

$$\alpha(e_{15} + e_{31}) A_r + (e_{33}\alpha^2 - e_{15}) A_z$$

$$+ (\varepsilon_o^{\varkappa}_{11} - \varepsilon_o^{\varkappa}_{33}\alpha^2) A_\phi = 0 \tag{25c}$$

where $v = \frac{\omega}{k}$ is the radial wave velocity. This is a linear set of homogenous equations. For a non-trivial solution, the determinant of the coefficient

matrix for A_r, A_z, and A_ϕ must vanish. The result is

$$|a_{ij}| = \begin{vmatrix} \rho v^2 - C_{11} + C_{44}\alpha^2 & -\alpha(C_{44}+C_{13}) & -\alpha(e_{15}+e_{31}) \\ \alpha(C_{44}+C_{13}) & \rho v^2 - C_{44}+C_{33}\alpha^2 & e_{33}\alpha^2 - e_{15} \\ \alpha(e_{15}+e_{31}) & e_{33}\alpha^2 - e_{15} & \varepsilon_o^{\varkappa}{}_{11} - \varepsilon_o^{\varkappa}{}_{33}\alpha^2 \end{vmatrix} = 0 \quad (26)$$

where a_{ij} is a typical element of the coefficient matrix.

When expanded, this secular equation yields three roots for α^2. If all three roots are real, the positive results of $\alpha_i = \pm (\alpha_i^2)^{\frac{1}{2}}$ are retained since negative values of α would result in infinite displacements and fields as z approaches minus infinity.

The other possibility is one real and two complex conjugate roots for α^2. Again, because of physical arguments, the real root with a positive value is retained along with the complex conjugate pair with positive real parts. Synge (27) refers to a plane wave with these decay characteristics as the generalized surface wave.

Using the three decay constants, Equations 24 can be rewritten as

$$u_r = B_1(kr)\{Ae^{\alpha_1 kz} + Be^{\alpha_2 kz} + Ce^{\alpha_3 kz}\} e^{j\omega t} \quad (27a)$$

$$u_z = B_o(kr)\{De^{\alpha_1 kz} + Ee^{\alpha_2 kz} + Fe^{\alpha_3 kz}\} e^{j\omega t} \quad (27b)$$

$$\phi = B_o(kr)\{Ge^{\alpha_1 kz} + He^{\alpha_2 kz} + Ie^{\alpha_3 kz}\} e^{j\omega t} \quad (27c)$$

where A through I are constants to be determined. These nine constants can be reduced to three by using Cramer's rule.

Since each of the terms involving α_1 alone must satisfy Equation 21

(disregarding the α_2 and α_3 terms for the present), the following relations result when Equations 27 are put into Equations 21:

$$a_{11}^1 A + a_{12}^1 D + a_{13}^1 G = 0 \tag{28a}$$

$$a_{21}^1 A + a_{22}^1 D + a_{23}^1 G = 0 \tag{28b}$$

where the a_{ij}^1 correspond to the elements of Equation 26 and the superscript 1 means α_1 appears in place of α in these elements. Similar equations corresponding to the α_2 and α_3 roots can be written:

$$a_{11}^2 B + a_{12}^2 E + a_{13}^2 H = 0 \tag{29a}$$

$$a_{21}^2 B + a_{22}^2 E + a_{23}^2 H = 0 \tag{29b}$$

and

$$a_{11}^3 C + a_{12}^3 F + a_{13}^3 I = 0 \tag{30a}$$

$$a_{21}^3 C + a_{22}^3 F + a_{23}^3 I = 0 \tag{30b}$$

If Cramer's rule (32) is applied to Equations 28, 29, and 30, the number of constants in Equations 27 reduce to three. A typical relation between the constants using Equations 28 would be:

$$A = \frac{\begin{vmatrix} -a_{13}^1 G & a_{12}^1 \\ -a_{23}^1 G & a_{22}^1 \end{vmatrix}}{\begin{vmatrix} a_{11}^1 & a_{12}^1 \\ a_{21}^1 & a_{22}^1 \end{vmatrix}} = M_{11} G \tag{31}$$

while the other constants are

$$B = M_{12}H, \quad C = M_{13}I, \quad D = M_{21}G, \quad E = M_{22}H, \quad F = M_{23}I \qquad (32)$$

Substituting the relationships of Equations 31 and 32 into Equations 27 eliminates six arbitrary constants and the solutions simplify to

$$u_r = B_1(kr)\{M_{11}Ge^{\alpha_1 kz} + M_{12}He^{\alpha_2 kz} + M_{13}Ie^{\alpha_3 kz}\}\, e^{j\omega t} \qquad (33a)$$

$$u_z = B_o(kr)\{M_{21}Ge^{\alpha_1 kz} + M_{22}He^{\alpha_2 kz} + M_{23}Ie^{\alpha_3 kz}\}\, e^{j\omega t} \qquad (33b)$$

$$\phi = B_o(kr)\{Ge^{\alpha_1 kz} + He^{\alpha_2 kz} + Ie^{\alpha_3 kz}\}\, e^{j\omega t} \qquad (33c)$$

Another relationship between the velocity and decay constants of Equation 28 can be obtained from the boundary conditions. Also, the boundary conditions allow a further reduction in the number of arbitrary constants in the above equations. The boundary conditions to be used are

1. Continuous electric potential across the boundary z = 0,

$$\phi(0^+) = \phi(0^-) .$$

2. Continuous normal component of the electric flux density,

$$D_z(0^+) = D_z(0^-) .$$

3. All normal components of stress at the surface are zero,

$$T_{rz} = T_{\theta z} = T_{zz} = 0.$$

Before applying the boundary conditions, however, it is necessary to obtain a solution for Equation 22, the governing equation for the fields outside the piezoelectric material. The solution for z > 0 is of the form

$$\phi = L\, B_o(kr)\, e^{(-\beta kz + j\omega t)} \qquad (34)$$

where L is an arbitrary constant and $\beta = 1$ is the decay constant in

free space (29).

Application of the boundary conditions to Equations 33 and 34

produces the following set of linear homogenous equations which are

represented in matrix form:

$$
\begin{bmatrix}
\{C_{44}(M_{11}\alpha_1 - M_{21}) & \{C_{44}(M_{12}\alpha_2 - M_{22}) & \{C_{44}(M_{13}\alpha_3 - M_{23}) \\
\quad -e_{15}\} & \quad -e_{15}\} & \quad -e_{15}\} \\
\\
\{M_{11}C_{13} & \{M_{12}C_{13} & \{M_{13}C_{13} \\
\quad +\alpha_1(M_{21}C_{33}+e_{33})\} & \quad +\alpha_2(M_{22}C_{33}+e_{33})\} & \quad +\alpha_3(M_{23}C_{33}+e_{33})\} \\
\\
\{M_{11}e_{31}+M_{21}e_{33}\alpha_1 & \{M_{12}e_{31}+M_{22}e_{33}\alpha_2 & \{M_{13}e_{31}+M_{23}e_{33}\alpha_3 \\
\quad -\epsilon_0(\kappa_{33}\alpha_1+1)\} & \quad -\epsilon_0(\kappa_{33}\alpha_2+1)\} & \quad -\epsilon_0(\kappa_{33}\alpha_3+1)\}
\end{bmatrix}
\begin{bmatrix} G \\ \\ H \\ \\ I \end{bmatrix} = 0 \quad (35)
$$

Again, the determinant of the coefficient matrix must be zero for

non-trivial solutions. Representing the above coefficient matrix by

$[b_{ij}]$ we must have

$$|b_{ij}| = 0 \qquad (36)$$

From this characteristic equation, a second relationship between velocity

and decay constants can be obtained. In theory it is possible to solve

Equations 26 and 36 for these needed values. However, in practice the

algebraic difficulties are practically insurmountable. These are avoided

by using numerical methods to be described later.

Equation 36 also allows the final form of the displacement and

potential solutions to be written when used with the following relationship

from the theory of systems of linear equations (32):

$$x_i = N(-1)^{i+1}|B_i|, \quad i = 1,2,3 \qquad (37)$$

where x_i represents the arbitrary amplitude constants of Equation 35,

i.e., G, H, and I. N is an arbitrary scalar constant, $|B_i|$ is the

determinant of the matrix $[B_i]$ which is obtained from $[b_{ij}]$ above by

deleting the last row and i^{th} column.

Applying Equation 37 to Equation 35 reduces the number of arbitrary

amplitude constants to one.

$$G = N(b_{12}b_{23}-b_{13}b_{22}) = n_1N \qquad (38a)$$

$$H = -N(b_{11}b_{23}-b_{13}b_{21}) = n_2N \qquad (38b)$$

$$I = N(b_{11}b_{22}-b_{12}b_{21}) = n_3N \qquad (38c)$$

Equations 33 and 38 combine to give the final form of the solutions

for particle displacement and electric potential for $z < 0$.

$$u_r = B_1(kr)N\{M_{11}n_1e^{\alpha_1 kz} +M_{12}n_2e^{\alpha_2 kz} +M_{13}n_3e^{\alpha_3 kz}\} \, e^{j\omega t} \qquad (39a)$$

$$u_z = B_0(kr)N\{M_{21}n_1e^{\alpha_1 kz} +M_{22}n_2e^{\alpha_2 kz} +M_{23}n_3e^{\alpha_3 kz}\} \, e^{j\omega t} \qquad (39b)$$

$$\phi = B_0(kr)N\{n_1e^{\alpha_2 kz} +n_2e^{\alpha_2 kz} +n_3e^{\alpha_3 kz}\} \, e^{j\omega t} \qquad (39c)$$

Using Equation 3 on Equation 39c produces the final form of the electric

fields for $z < 0$:

$$E_r = B_1(kr)kN\{n_1e^{\alpha_1 kz} +n_2e^{\alpha_2 kz} +n_3e^{\alpha_3 kz}\} \, e^{j\omega t} \qquad (40a)$$

$$E_z = -B_0(kr)kN\{\alpha_1 n_1e^{\alpha_1 kz} +\alpha_2 n_2e^{\alpha_2 kz} +\alpha_3 n_3e^{\alpha_3 kz}\} \, e^{j\omega t} \qquad (40b)$$

For z > 0 the final forms of the solutions are

$$\phi = B_o(kr)N(n_1+n_2+n_3) \; e^{(-kz+j\omega t)} \tag{41a}$$

$$E_r = B_1(kr)kN(n_1+n_2+n_3) \; e^{(-kz+j\omega t)} \tag{41b}$$

$$E_z = B_o(kr)kN(n_1+n_2+n_3) \; e^{(-kz+j\omega t)} \tag{41c}$$

The mathematical model for the electric fields and particle displacements is, therefore, complete. The next section will describe a numerical application of the above equations for a lead-zirconate-titanate ceramic selected for the experimental portion of the research.

2. Computer solution for PZT-5A

The lead-zirconate-titanate ceramic PZT-5A was selected as the piezoelectric material to be used for the computational and experimental portions of the research. The physical properties of PZT-5A that are important to this study are listed in Table 1.

The numerical analysis was based on the procedure suggested by Tseng and White (29). The physical constants for PZT-5A from Table 1 were entered into Equation 26. This equation then contains only the undefined variables of velocity, v, and decay, α. A phase velocity is assumed and substituted into Equation 26. With the aid of a computer, the six roots of α were determined. Three of these roots and the velocity were used in the boundary condition determinant, Equation 35, to see if this equation was satisfied. If not, a new velocity was selected and the process repeated until the boundary condition determinant was satisfied. In practice, it was not necessary to satisfy Equations 26 and 35 exactly

because the number of significant figures required to do so far out-
numbered the significant figures obtainable from any physical measurement.
Therefore, the approximation to be described later was used.

Two computer programs were used in the numerical analysis. The
roots of the decay constant from Equation 26 were found with the aid
of an IBM-360G program written by Deckert and Johnson (9). This linear
systems analysis (LISA) program allows the solution to be obtained for
systems of linear equations that have coefficient matrices with polynomial
elements. A glance at the coefficient matrix, Equation 25, reveals
polynomial elements for the decay constant, α. Therefore, this flexible
program permits a simple solution for the decay roots once the material
constants and phase velocity are given.

A second program was written to test the decay constants obtained
from LISA. Using a complex format, this Fortran program began with the
material constants, assumed velocity, and decay constants from LISA and
calculated the value of the determinant of the coefficient matrix from
Equation 35.

As was noted in the opening paragraphs of this section, an iteration
on the value of phase velocity was necessary to find the correct combin-
ation of velocity and decay constants to solve Equation 26 and 35
simultaneously. The four values of velocity used during the iteration
process are plotted in Figure 4 showing how the imaginary part of the
boundary condition determinant varies. This value goes through zero
for a phase velocity of approximately 1980 meters/second. Smaller velocity
increments were then selected and the imaginary part of the above deter-
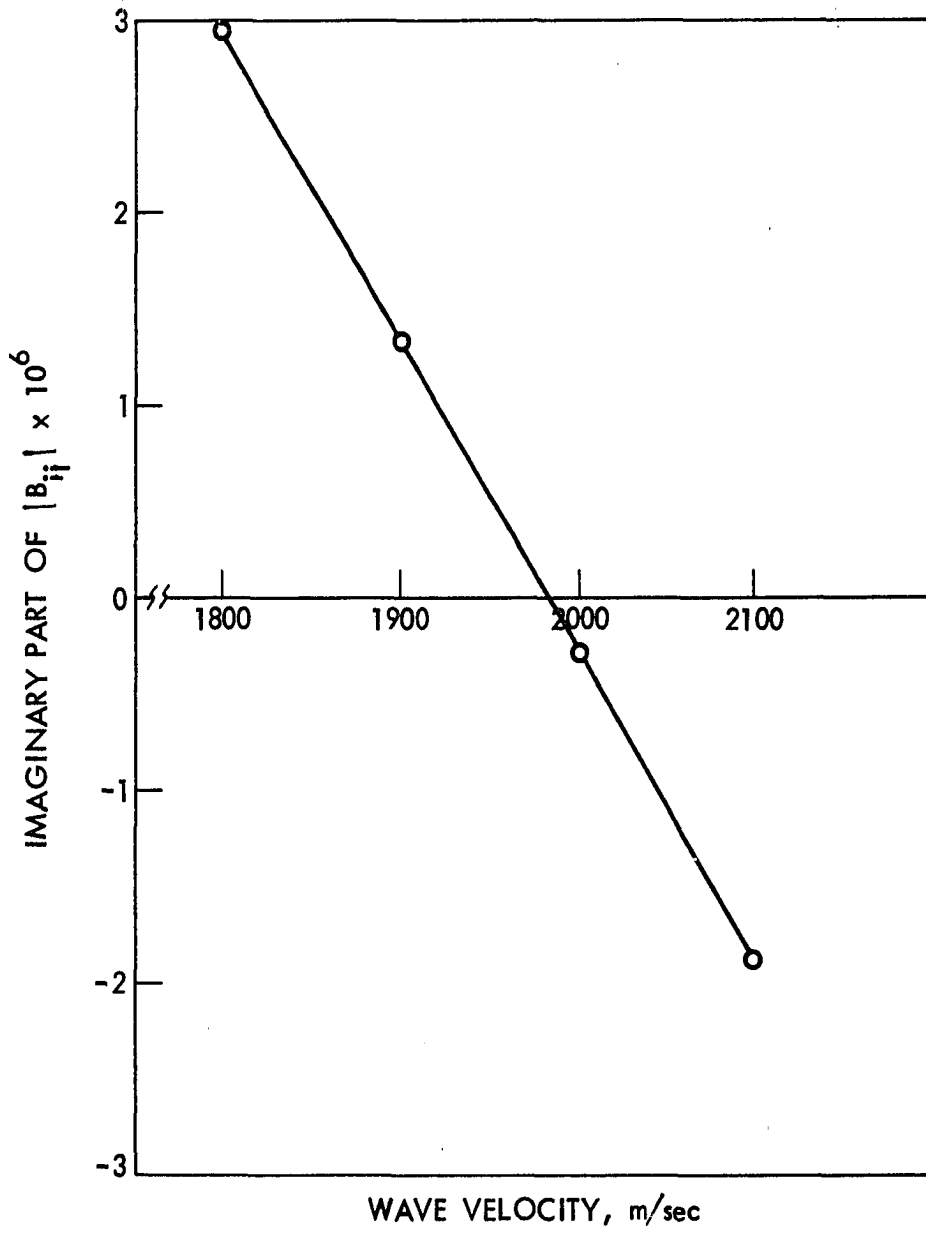
Fig. 4. Plot used to approximate theoretical wave velocity.

minant was observed to change sign at approximately 1982 meters/second.
A more accurate determination of velocity could not be justified in view
of the fact that material constants are given to only three significant
figures at best. Also, experimental velocity measurements could only
be carried out to the third significant figure.

The results of the numerical analysis are as follows:

phase velocity - v = 1982 meters/second

decay constants - α_1 = 1.078

α_2 = 0.6258 - j0.3461

α_3 = 0.6258 + j0.3461

An important part of the second program was to calculate the
constants for the final solutions represented by Equations 39, 40, and
41. These equations have been simplified by single letter substitutions
for the products and sums of amplitude constants and are rewritten
below. For z < 0

$$u_r = B_1(kr)N \exp(j\omega t) \sum_{i=1}^{3} p_{1i} \exp(\alpha_i kz) \qquad (42a)$$

$$u_z = B_0(kr)N \exp(j\omega t) \sum_{i=1}^{3} p_{2i} \exp(\alpha_i kz) \qquad (42b)$$

$$\phi = B_0(kr)N \exp(j\omega t) \sum_{i=1}^{3} n_i \exp(\alpha_i kz) \qquad (42c)$$

$$E_r = B_1(kr)kN \exp(j\omega t) \sum_{i=1}^{3} n_i \exp(\alpha_i kz) \qquad (42d)$$

$$E_z = B_0(kr)kN \exp(j\omega t) \sum_{i=1}^{3} p_{3i} \exp(\alpha_i kz) \qquad (42e)$$

For $z > 0$ the solutions have the form

$$\phi = B_o(kr)Nn \ \exp(j\omega t - kz) \tag{43a}$$

$$E_r = B_1(kr)Nn \ \exp(j\omega t - kz) \tag{43b}$$

$$E_z = B_o(kr)Nn \ \exp(j\omega t - kz) \tag{43c}$$

where $n = n_1 + n_2 + n_3$. The velocity, decay, and amplitude constants for the above equations are summarized in Table 2.

This concludes the numerical analysis for PZT-5A. The experimental section describes an investigation which has the purpose of checking the validity of the above mathematical model for radial surface waves.

Table 2. Velocity, decay, and amplitude constants for radial surface waves on the free surface of PZT-5A. Constants represented here correspond to Equation 42 and 43.

| Constant	Value from numerical analysis
V(meters/second)	1982
α_1	1.078
α_2, α_3	$0.6258 \mp j0.3461$
P_{11}	$j0.2554 \times 10^{-8}$
P_{12}, P_{13}	$(\pm 12.77 - j3.811) \times 10^{-8}$
P_{21}	$-j0.2377 \times 10^{-8}$
P_{22}, P_{23}	$(\mp 14.08 - 5.006) \times 10^{-8}$
P_{31}	$j11.34$
P_{32}, P_{33}	$\mp 148.4 + j56.36$
n_1	$j10.52$
n_2, n_3	$\mp 220.2 - j31.73$
n	$- j52.94$

III. EXPERIMENTAL INVESTIGATION

Radial surface waves are unique in one respect when compared to plane waves or straight crested waves discussed by others (25, 29). It is possible to simulate the theoretical situation of radial waves exactly with experimental techniques because transducers are circular. Plane waves on the other hand, cannot be produced exactly as the theory assumes because finite width transducers must be used. As a result of this physical limitation on the transducer, plane waves diverge somewhat as they propagate away from the transmitter. This produces higher insertion loss. Insertion loss, phase velocity, and bandwidth are included in the topics to be discussed in the next sections.

A. Description of Experiments

Two devices were constructed in accordance with the procedure given in the appendix. The difference between the two was in the number of electrodes used in the outer transducer set. Figure 5 shows two views of device number one with one electrode pair each for the receive and transmit transducers. The piezoelectric substrate is a disc of PZT-5A measuring $2\frac{1}{2}$ inch in diameter and $\frac{1}{2}$ inch in thickness. This obviously does not approach the theoretically assumed semi-infinite substrate, but, by properly designing the electrodes, measurements can be made without the finite boundaries causing significant interference.

The center-to-center spacing of the copper electrodes shown in Figure 5 measures 0.020 inch corresponding to the half wavelength of a radial surface wave for a frequency of approximately 2 MHz. The electrodes
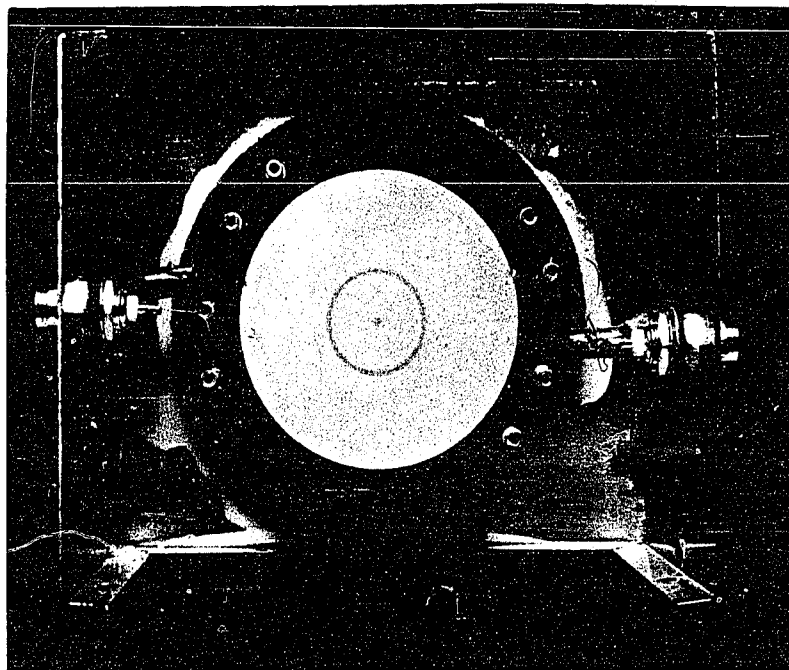
(a)
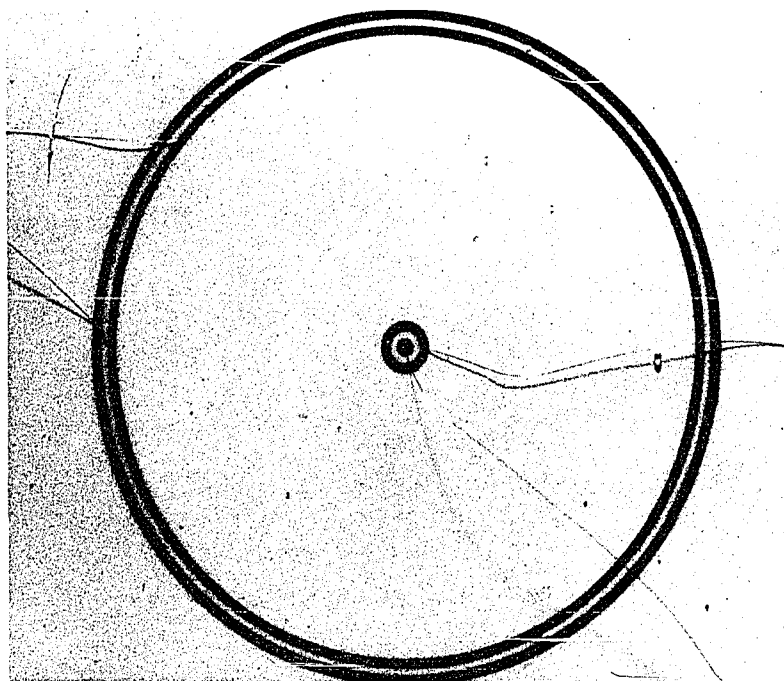
(b)

Fig. 5. Device 1. PZT-5A disc with two-electrode transmit and receive.

are about 10,000 Å in thickness. The distance between the center of

the outer ring of the inner electrode pair and the center of the inner

ring of the outer electrode pair is 0.385 inch. This is an important

distance that will be used with delay time measurements to determine

phase velocity.

Electrical interference was minimized by placing each device in a

metal container such as the one shown in Figure 5a. Connections to the

outside were made through BNC feed-through connectors.

Figure 6 shows device number two. It was constructed from the same

master drawing as number 1 after four electrodes were added, two inside and

two outside the outer pair shown in Figure 5, giving a total of 6 electrodes

for the outer transducer. The center-to-center spacing between each pair

and the electrode thickness remains the same as that of device number 1.

However, adding two electrodes closer to the center reduces the wave

propagation distance from 0.385 inch to 0.345 inch.

Electrical connections were made to each copper electrode by gold

wire using an ultrasonic bonder. Figure 6b shows a close-up view of

device 2 and the lead connections that were made to the outer transducer

set.

The two circuit configurations used during the device tests are

shown in Figure 7. By having the switch in position 1 it was possible

to gate a narrow band signal through the coupler to the transmit electrodes.

The gate width and signal frequency were controlled independently. Switch

position 2 placed the output of the pulse generator directly across the

transmitting transducer. This provided a broad sprectum of frequencies
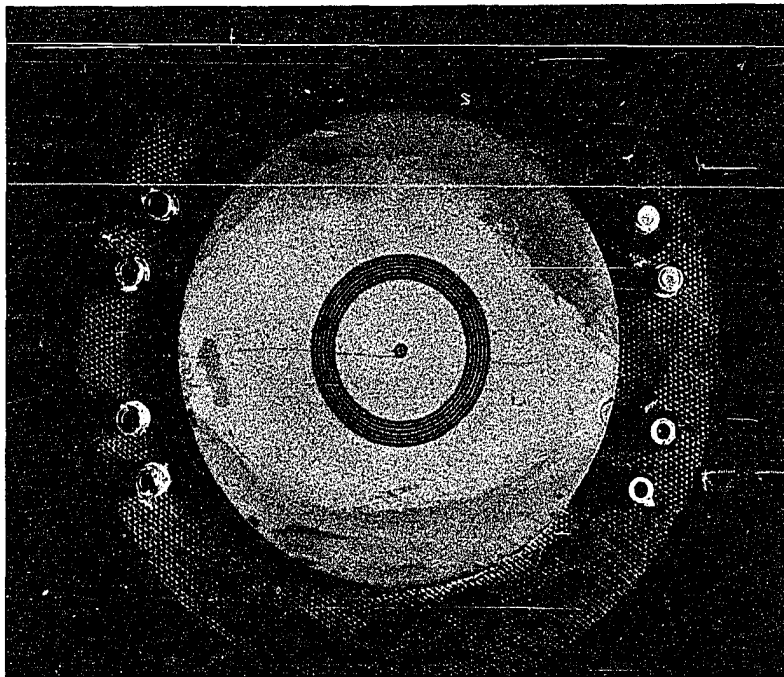
(a)
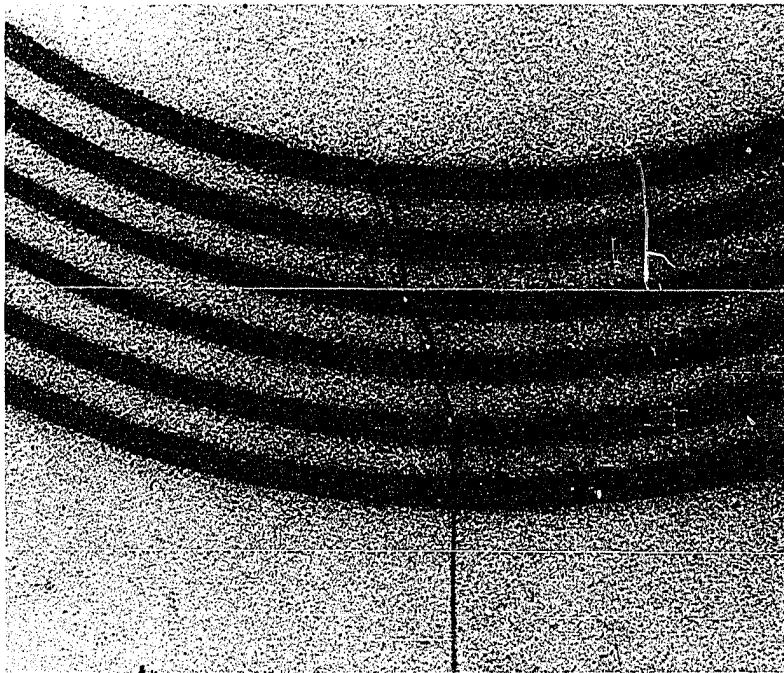
(b)

Fig. 6. Device 2. (a) Composite view. (b) Outer electrodes with electrical connections made by ultrasonic bonder.
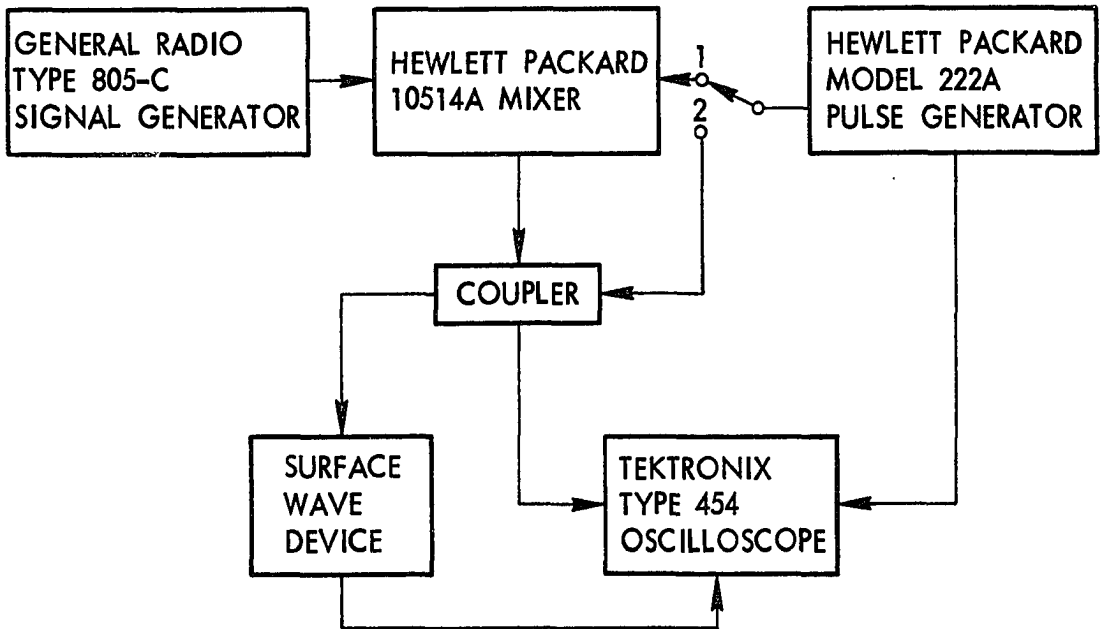
Fig. 7. Experimental instrumentation. Switch positions:
(1) narrowband and (2) broadband.

and allowed the transducers to respond at their natural resonant

frequency.

The test setup included a Tektronix type 454 oscilloscope that has

a bandwidth of 150 MHz. Voltage insertion loss, delay time, and band-

width were measured with the aid of this instrument.

B. Results of Tests

Velocity provides the basis for checking the mathematical model

presented in Chapter II. Using the electrode separation distance given

in the previous section and an accurate measurement of time delay, it is

possible to compute velocity to three significant figures.

The narrowband and broadband techniques described in Section A were

employed in the time delay measurements. Figure 8 shows the results of

applying a narrowband signal to each device. A 1.65 MHz signal that

was 2 μsec in time length was gated into the outer electrodes. A portion

of this signal couples into the output circuitry and appears in the first

2 μsec of each photograph. The radial surface wave begins after 4.5 μsec.

Individual cycles cannot be seen in the photographs because the oscillo-

scope synchronization was taken from the pulse generator. Time delay

taken from Figure 8, propagation distance, and velocity are summarized

in Table 3.

Table 3. Summary of experimental velocity measurements.

Device	Time Delay μsec	Distance inch	Velocity m/sec
1	4.90	0.385	2000
2	4.70	0.345	1870
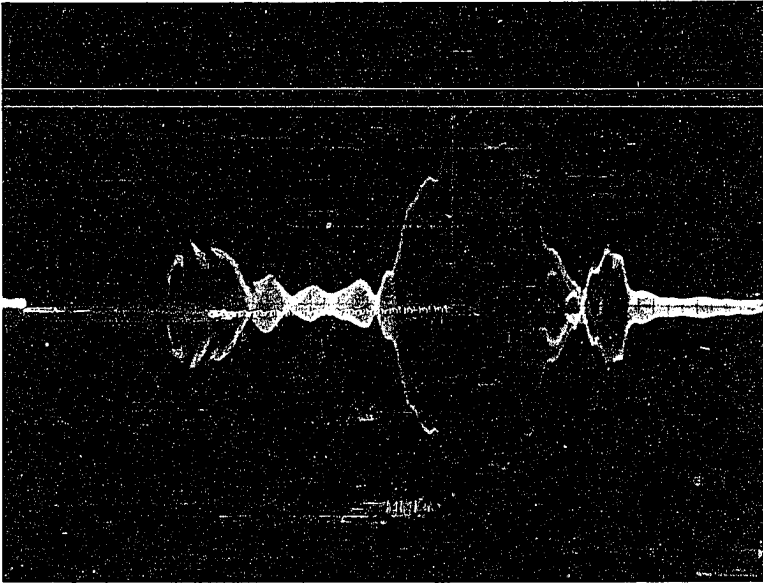
(a) Device 1. Vertical — 10 mV/cm; Horizontal — 1 μsec/cm
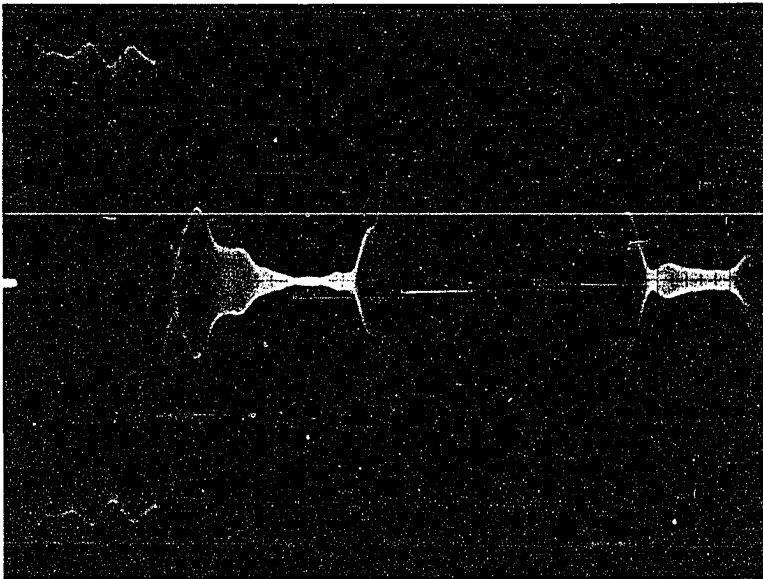
(b) Device 2. Vertical — 20 mV/cm; Horizontal — 1 μsec/cm

Fig. 8. Results of applying 1.65 mHz, 2 μsec gated signal to outer
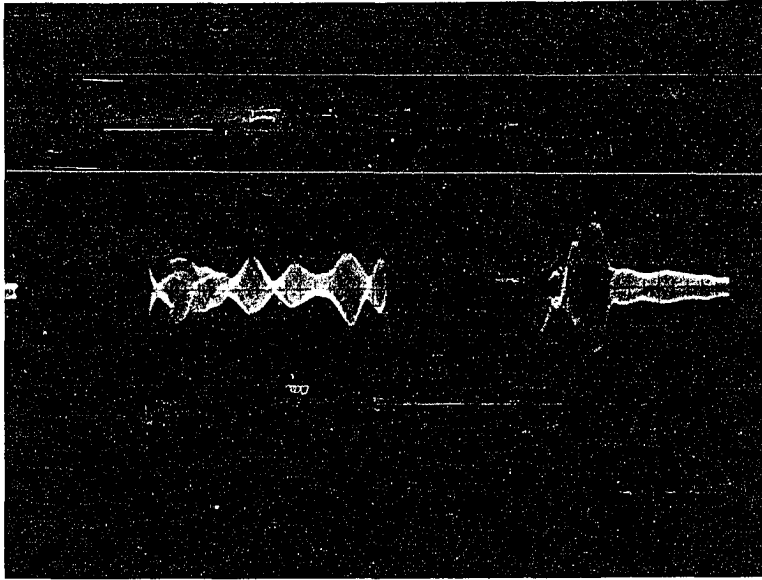electrodes of each device.

As one might expect, radial wave transducer sets with different radii will not produce surface waves of the same magnitude. Applying an electrical signal to the outer electrodes results in a larger wave at the inner transducer than when the role of the electrodes is reversed. Figures 9 and 10 demonstrate this phenomenon for both devices. In each case the signal level is improved approximately 5 times by using the outer transducer set for transmitting instead of the inner electrodes.

The maximum voltage ratio, output divided by input, for radial wave transducers can obviously be achieved with the arrangement that uses the outer electrodes to transmit and inner electrodes to receive. The same conclusion could be drawn for insertion loss since it is related to the voltage ratio. Figure 11 shows the input and output voltage signals for device 2. For an input of 1 volt peak-to-peak the output is approximately 0.32 volt or down about 10 db.

Bandwidth was measured along with the above voltage ratio. A frequency change of 0.52 MHz was achieved while keeping the signal level within the half-power points. For a center frequency of 1.65 MHz this bandwidth represents about a 30 percent change in frequency for device 2.

Application of a broadband pulse reveals the existence of other propagation mode groups due to the finite boundaries. Figure 12 shows the response of each device to a 10 volt 20 nsec wide pulse. The radial mode begins in each case at just over 4.4 μsec. The signal in the middle trace of each photograph that begins at approximately 2.4 μsec corresponds to the velocity of bulk waves in PZT-5A. A signal that propagates radially outward from the outer electrodes, reflects off the edge of
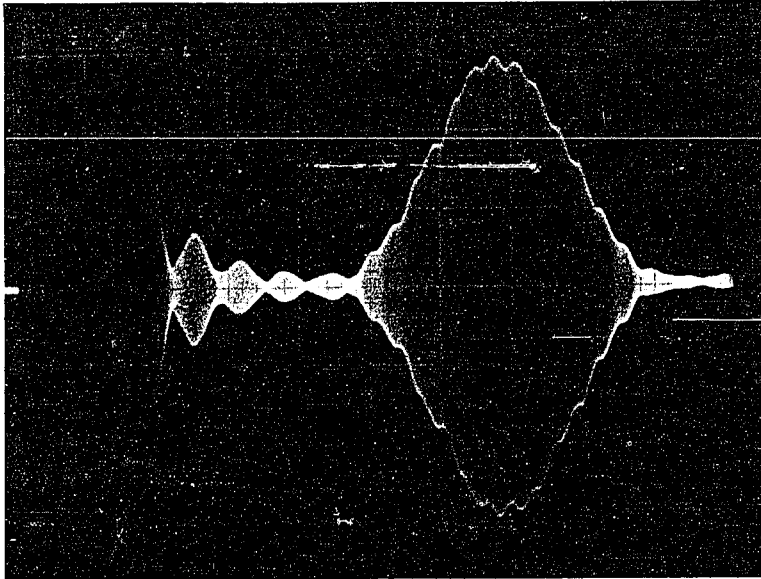
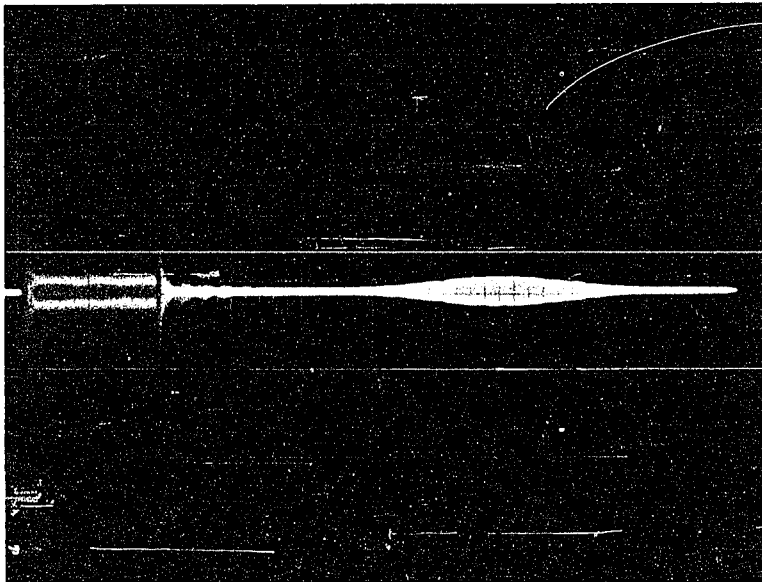(a)   Outer electrode transmit.
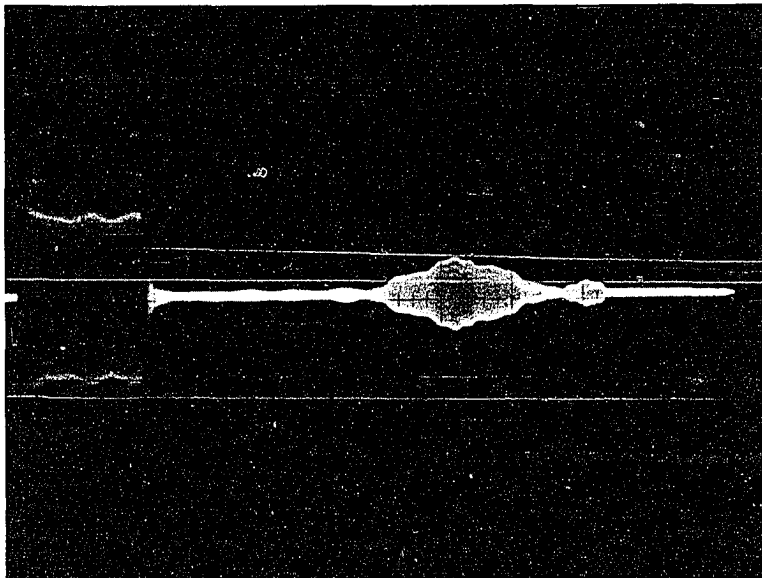
(b) Inner electrode transmit.

Fig. 9.   Comparison of signals produced by outer and inner electrodes
          on device 1.   Scale factors for each photograph: vertical —
          10 mV/cm; horizontal — 1 μsec/cm.

(a) Outer electrode transmit.

(b) Inner electrode transmit.

Fig. 10. Comparison of signals produced by outer and inner electrodes
on device 2. Scale factors for each photograph: vertical —
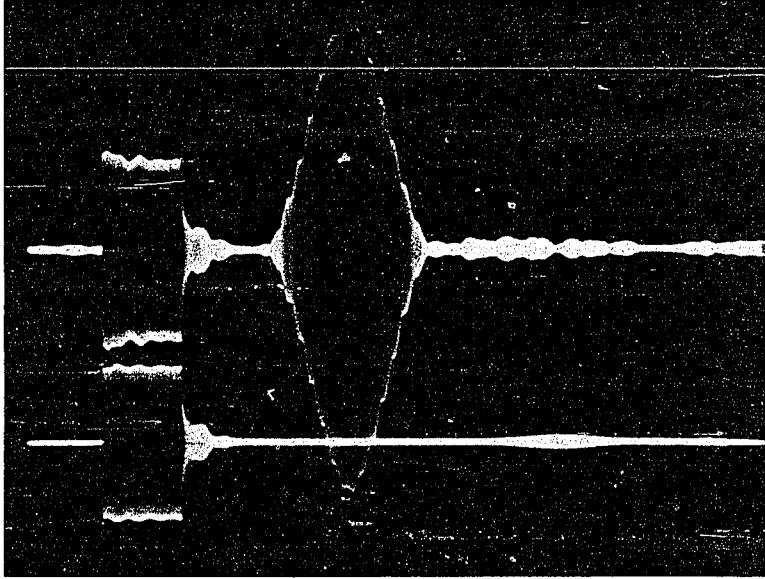10 mV/cm; horizontal — 1 μsec/cm.

Fig. 11. Input (bottom) and output (top) for device 2 arranged for
outer electrode transmit. Scale factors: vertical —
top 50 mV/cm, bottom 0.5 V/cm; horizontal — 2 μsec/cm.
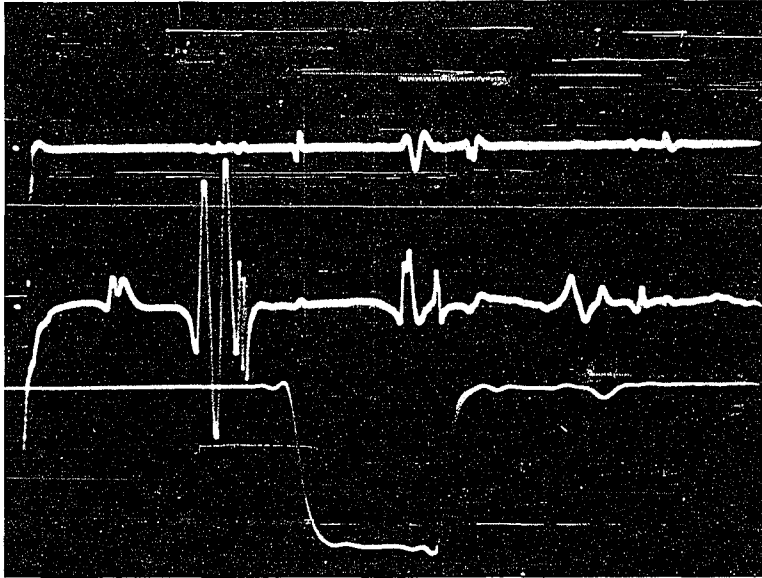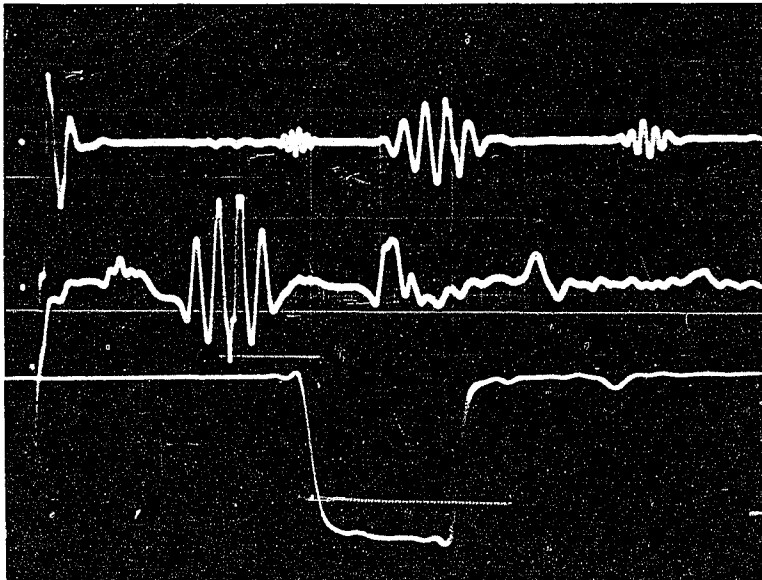
(a) Device 1.

(b) Device 2.

Fig. 12. Response to 20 nsec pulse applied to the outer electrodes.
For each device: top trace — signals on outer electrodes;
middle trace — signals on inner electrodes; bottom trace —
applied signal. Scale factors for each photograph: vertical —
top and center 20 mV/cm, bottom 5 V/cm; horizontal — top and
center 2 μsec/cm, bottom 10 nsec/cm.

the disc, and travels back to the transmit electrode can be observed at about 18 μsec in the top trace of each photograph. Other signals result from bulk waves that reflect off the bottom of the disc.

Another interesting response pattern appears at slightly over 10 μsec in the top trace of Figure 12b and is just visible at the same time in Figure 12a. This signal is produced at the transmit electrode set after the wave has passed under the receive electrodes, converged at the center, and then propagates from the center outward. Figure 13 compares the amplitude of this signal (11 μsec on bottom trace) with the main radial mode sensed by the receive electrodes (4.8 μsec on top trace). Each trace has a vertical sensitivity of 50 mv/cm so for the 1 volt input the main signal suffers a loss of 10 db while the wave sensed by the transmit electrodes is down by 33 db.

One last interesting phenomenon related to the number of electrodes is demonstrated in Figure 14. Here the applied signal has been extended in time to 4 μsec but the receive signal builds up to a maximum in slightly less than 2 μsec and remains at this level even though the input pulse length is longer. This is due to the reenforcement produced by the six electrodes used for the transmit transducer of device 2. Each pair of electrodes produces a wave that propagates radially away and reinforces the waves generated by adjacent pairs. Approximately 2 μsec are required for this device to reach a maximum signal level corresponding to the time required for a wave to pass from the outer side of the transmit electrodes to the inner side.
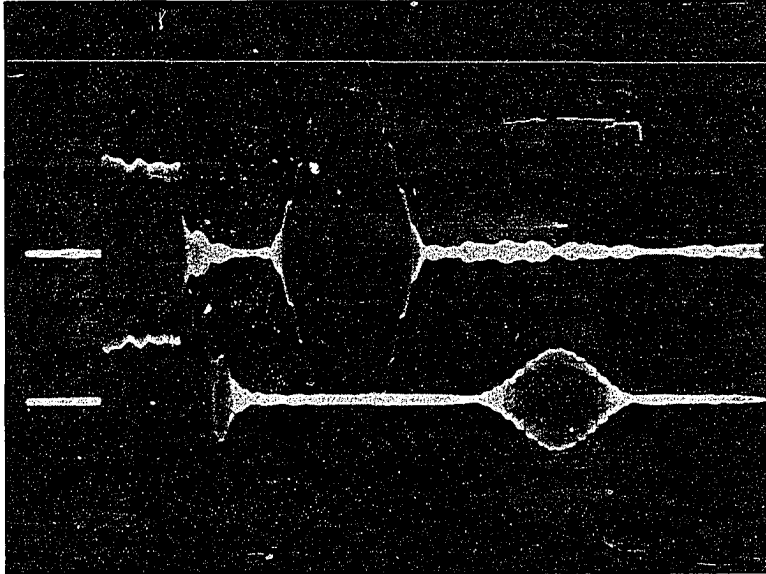
Fig. 13. Comparison of main signal received by inner (top) and outer
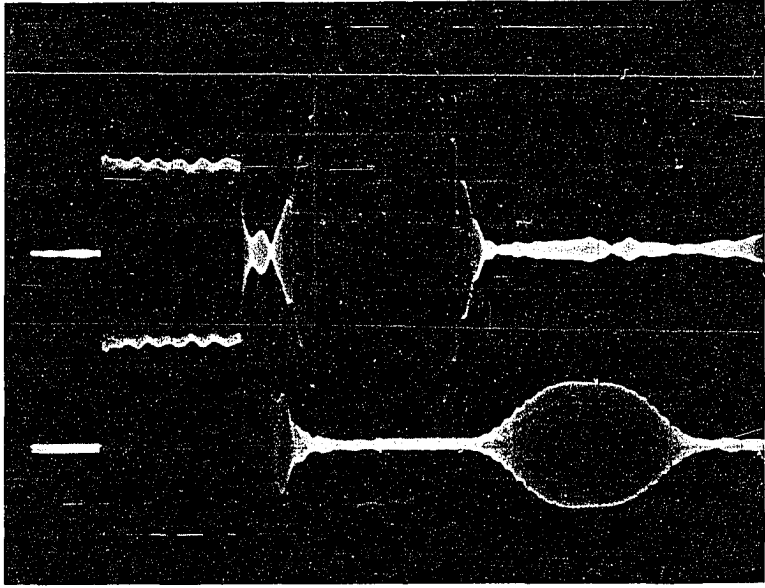(bottom) electrodes. Vertical — 50 mV/cm; Horizontal —
2 μsec/cm.

Fig. 14. Demonstration of amplitude build-up due to multiple electrodes of device 2.

C. Discussion of Results

Phase velocity was determined experimentally for both devices used during the study. These values differed by 130 m/sec from each other and by about 20 m/sec and 110 m/sec from the theoretical value of 1982 m/sec found in Chapter II. The source of these variations was two fold. First, it was difficult to get an accurate measurement of the path length traveled by the wave and second, some difficulty was experienced in reading the delay times off the oscilloscope. The error resulting from each of these could be reduced by making smaller transducer electrodes and operating at higher frequencies. However, PZT-5A is a polycrystalline ceramic and higher frequency operation would be limited by the grain size and porosity since losses go up due to scattering. For operation at higher frequencies it would be necessary to select a good single crystal with transverse isotropy such as ZnO or CdS.

The expected improvements in unidirectional transducer characteristics discussed in Section I B were not fully realized during the experiments. There were indications that insertion loss could be reduced by using radial wave transducers instead of planar devices. However, the best characteristics were obtained by using large radii transducer sets to transmit inward instead of transmitting with electrodes at the center as suggested in the opening section. The measured voltage ratio was low when using the outer electrodes for transmitting and this suggests a low insertion loss could also be achieved. An involved study of transducer impedance characteristics required to make meaningful statements about insertion loss was not the purpose of this research.

The fact that larger amplitude signals were received by the single pair of electrodes at the center of each device can be explained by considering the small argument limit of the Hankel functions (11) describing radial wave propagation. The magnitudes of these functions tend to infinity for small radius, r, according to log (r) for the zero order function and 1/r for the first order function. Therefore, the large amplitude displacements and electric fields leading to the signals received by the center electrodes are predicted by the theory of Chapter II.

Tseng (28) provides a theoretical analysis of the bandwidth for interdigital transducers and concludes that the bandwidth, ΔF, number of electrodes, N, and center frequency, f_o, are related by

$$\Delta F = \frac{2}{N} f_o .$$ (44)

If this holds for radial transducers it suggests a bandwidth of (2/6) x 1.65 MHz or 0.55 MHz. The measured value of bandwidth was 0.52 MHz so Tseng's approximation apparently holds for radial surface waves.

IV. SUMMARY AND CONCLUSIONS

Radial surface waves have been described theoretically by constructing a mathematical model for electric fields and particle displacements based on Newton's second law and Maxwell's equations in curvilinear coordinates. Using this model, a computer solution was obtained for PZT-5A. As part of the solution, a phase velocity of 1982 m/sec was predicted for radial surface waves on a PZT-5A substrate.

An experimental investigation was conducted with the purpose of testing the mathematical model. Copper electrodes were deposited on PZT-5A and radial surface waves were generated at a frequency of 1.65 MHz. Two devices were constructed and used to determine phase velocity, the output-to-input voltage ratio, and bandwidth. The measured values of phase velocity were 1% high for one device but 5.5% low for the other when compared to the theoretically predicted value given above. Difficulty was experienced with making both the time and distance measurements needed for accurate velocity calculations. Higher frequency would allow each of these measurements to be improved.

The theory of Chapter II suggests that concentric radial wave transducer sets would have different insertion loss characteristics depending on whether waves propagate inward or outward. Experiments confirmed this when it was determined that the output-to-input voltage ratio was approximately 5 times greater for inward traveling waves than for outward traveling waves.

The experiments indicated that more efficient devices could be

constructed using radial surface waves. A bandwidth of 30 percent was obtained while the signal voltage level dropped by only 10 db for the propagating wave.

V. LITERATURE CITED

1. Adler, R. B., Chu, L. J., and Fano, R. M. Electromagnetic Energy Transmission and Radiation. Wiley, New York. 1960.

2. Aris, R. Vectors, Tensors, and the Basic Equations of Fluid Mechanics. Prentice-Hall, Englewood Cliffs, N. J. 1962.

3. Berlincourt, D. A., Curran, D. R., and Jaffe, H. Piezoelectric and piezomagnetic materials and their function in transducers. In Physical Acoustics. Mason, W. P., ed. Vol. IA. Pp. 169-270. Academic Press, New York. 1964.

4. Bradfield, G. Ultrasonic transducers--part A. Ultrasonics 8: 112-123. April 1970.

5. _____. Ultrasonic transducers--part B. Ultrasonics 8: 117-189. July 1970.

6. Budreau, A. J. and Carr, P. H. Surface wave attenuation at microwave frequencies: II temperature dependence. IEEE Ultrasonics Symposium Final Program. Pp. 21. October 1970.

7. Childs, W. H. Traveling wave energy conversion in piezoelectric media. Ph.D. dissertation. Iowa State University. 1970.

8. Collins, J. H., Gerard, H. M., Reeder, T. M., and Shaw, H. J. Unidirectional surface wave transducer. Proceedings of the IEEE (Letters) 57: 833-835. May 1969.

9. Deckert, K. L. and Johnson, E. T. LISA 360A-A program for linear systems analysis. IBM Corporation, Hawthorne, New York. 1968.

10. Ewing, W. M., Jardetzky, W. S., and Press, F. Elastic Waves in Layered Media. McGraw-Hill, New York. 1961.

11. Harrington, R. F. Time-Harmonic Electromagnetic Fields. McGraw-Hill, New York. 1961.

12. IRE Standards on Piezoelectric Crystals: Measurements of piezoelectric ceramics. Proceedings of IRE 49: 1161-1169. 1961.

13. Kittel, C. Introduction to Solid State Physics. Wiley, New York. 1967.

14. Koerber, G. G. Uncoupled piezoelectric surface-wave modes. IEEE Trans. Sonics and Ultrasonics SU-18: 73-78. April 1971.

15. Landolt, Hans Heinrich. *Zahlenwerte und Funktionen aus Naturwissenschaften und Technik*. Vol. 1. Springer-Verlag, Berlin. 1966.

16. _____. *Zahlenwerte and Funktionen aus Naturwissenschaften und Technik*. Vol. 2. Springer-Verlag, Berlin. 1969.

17. Lean, E. G. and Broers, A. N. Acoustic and transferred electron circuits. IEEE International Solid State Circuits Conference Technical Paper Digest 1970: 130-131. 1970.

18. Martin, G. E. Vibrations of longitudinally polarized ferroelectric cylindrical tubes. The Journal of the Acoustical Society of America 35: 510-520. April 1963.

19. Mason, W. P. *Crystal Physics of Interaction Processes*. Academic Press, New York. 1966.

20. Musgrave, M. J. P. *Crystal Acoustics*. Holden-Day, London. 1970.

21. Nye, J. F. *Physical Properties of Crystals*. Oxford Press, London 1957.

22. Rayleigh, Lord. On waves propagated along the plane surface of an elastic solid. London Mathematical Society Proceedings 17: 4-11. 1885.

23. Smith, A. B. and Damon, R. W. A bibliography of microwave ultrasonics. IEEE Trans. Sonics and Ultrasonics SU-17: 86-111. April 1970.

24. Smith, W. R., Gerard, H. M., Collins, J. H., Reeder, T. M., and Shaw, H. J. Design of surface wave delay lines with interdigital transducers. IEEE Trans. Microwave Theory and Techniques MTT-17: 865-873. November 1969.

25. Spaight, R. N. Piezoelectric and elastic surface waves on $LiNbO_3$. Ph.D. dissertation. Iowa State University. 1969.

26. Spiegel, M. R. *Vector Analysis*. Schaum Publishing Co., New York. 1959.

27. Synge, J. L. Elastic waves in anisotropic media. Journal of Mathematics and Physics 35: 323-334. 1957.

28. Tseng, C. C. Frequency response of an interdigital transducer for excitation of surface elastic waves. IEEE Trans. Electron Devices ED-15: 586-594. 1968.

29. Tseng, C. C. and White, R. M. Propagation of piezoelectric and elastic surface waves on the basal plane of hexagonal piezoelectric crystals. Journal of Applied Physics 38: 4274-4280. October 1967.

30. van den Heuvel, A. P. Surface-wave electronics. Science and Technology. Pp. 52-60. January 1969.

31. Worley, J. C. and Matthews. Broadband unidirectional surface wave transducer. IEEE Ultrasonics Symposium Final Program. Pp. 27. October 1970.

32. Wylie, C. R. Advanced Engineering Mathematics. McGraw-Hill, New York. 1960.

VI. ACKNOWLEDGEMENTS

It is a pleasure to express my sincere appreciation to Dr. George G. Koerber for his encouragement, ideas, and guidance throughout the course of my degree program.

Special thanks are extended to Dr. R. E. Post for the helpful suggestions and to Drs. R. C. Rosenfeld and R. E. Vogel for the discussions that resulted in so many valuable ideas.

Although my wife understands very little of the material within this thesis, I am indebted to her for the patience and understanding she has shown during my school years.

VII. APPENDIX

The purpose of this section is to provide a complete description of the procedure used to prepare PZT-5A for use during the experimental portion of the research. It was necessary to construct metal electrodes on the surface of this ceramic and then provide connections through which the electrical signals could be applied. Each of the steps leading to the finished surface wave device are described in the following paragraphs.

Transducer construction was accomplished in four major steps. They are (1) substrate preparation, (2) thin film deposition, (3) photo-masking and etching, and (4) electrical lead connection. These steps left the device ready for the experimental studies.

PZT-5A was purchased in $2\frac{1}{2}$ inch diameter and $\frac{1}{2}$ inch thick discs from the Clevite Corporation (Bedford, Ohio). The material was supplied with silver electrodes applied to the flat faces of the discs. In order to generate surface waves on a free surface (non-metalized), it was necessary to remove these silver conductors and polish the surface. This process included sanding to remove the bulk of the silver and then submersing the disk in a solution of 5 parts ammonium hydroxide and 3 parts (by volume) of 30% hydrogen peroxide. This technique allowed complete removal of the silver without damage to the surface of the PZT-5A.

The next step in the material preparation was to lap one face of the disk to eliminate surface scratches and irregularities in order to reduce attenuation of the propagating surface wave. The commercial Lapmaster 10, manufactured by the Crane Packing Company (Morton Grove, Illinois) was used in conjunction with Geoscience Microgrit aluminum

oxide as the lapping compound. The compounds were used with water to produce a slurry of various grit sizes. Twenty-five micron was used first for 5 minutes then the lapping machine was completely flushed out with water and 12 micron applied and used for 15 minutes. Smaller grit sizes were tried but without success. Twelve micron was determined to be adequate for the present program.

After lapping, each sample was washed using cotton balls and a liquid detergent and rinsed with distilled water. This was the final step preceding vacuum deposition of a thin film of metal on the surface that had been lapped.

A Consolidated Vacuum Corporation model LCI-18B vacuum system was used during the deposition portion of the transducer construction. Copper was selected as the metal to be used for the electrodes primarily because of its availability and ease with which it could be vacuum deposited. Nearly pure copper chunks measuring approximately 3/8" x 3/8" x 1/8" were placed in a tantalum boat within the vacuum chamber. The chamber was pumped down to approximately 5×10^{-6} millimeters of mercury before depositing copper. Heating of the copper chunks was accomplished with a Veeco Instrument Company electron beam gun system.

Copper was deposited at the rate of approximately 60 $\overset{\text{o}}{\text{A}}$ per second by controlling copper heating through the electron current. This rate and the subsequent thin film thickness were determined with the aid of a quartz crystal that was ajacent to the PZT-5A substrate in the vacuum chamber. The crystal was arranged in an oscillator circuit so that a frequency change of 5 Hz represented approximately one angstrom of copper

built up on the quartz surface. The frequency was observed on a Hewlett-Packard model 5216A digital counter so that deposition rate and total thickness could be monitored continuously. Copper thin film thicknesses of approximately 5,000 $\overset{o}{A}$ and 10,000 $\overset{o}{A}$ were tried during the investigation. The thicker deposition proved to be the most useful during the photo-mask and etching phases of the transducer construction.

When the PZT-5A substrates were removed from the vacuum chamber, unthinned liquid photo resist (Shipley Company positive AZ-111) was applied to the copper surface. The disc was shaken by hand to remove the excess liquid, placed on edge in a furnace set for $74^{o}C$, and allowed to dry for 20 minutes.

The next step was to expose the dried photo resist with a 200 watt mercury short arc lamp through a positive photo-mask. The mask contained blackened lines in the shape and position of the desired electrodes and was transparent everywhere else. It was made by photo reducing a master copy approximately 25 times. The mask was placed in contact with the photo resist and exposure lasted for 90 seconds.

The photo resist was then developed for 60 seconds in the Shipley Company type AZ-303 developer diluted with five parts water to one part developer. Pressurized air drying of the disk, copper, and developed photo resist followed the developing stage.

The final step in the electrode construction was to etch away all copper on the substrate which was not protected by unexposed photoresist. Etching was accomplished by placing the disc in a ferric chloride solution. This solution had been prepared by diluting a saturated solution of ferric

chloride approximately 10 times by adding water. Dilution slowed the copper etch and allowed more control over the process. After etching was complete, the surface was rinsed with water and then methyl alcohol to remove all of the unexposed photo resist so that electrical connections could be made to the copper.

Circuit connections were made with the Lindberg Hevi-duty Company (Mountain View, California) model 1100 ultrasonic stitchbonder. Gold (99.99%) wire with a diameter of 0.0007 inch was used for the electrical leads. Completion of this step of the procedure left the device ready for the experimental investigation.